CHARACTERIZATION AND APPLICATION OF MICROFLUIDIC DEVICES FOR STUDYING CELLULAR MIGRATION AND CHEMOTAXIS

by

LYNDON K. LEE

Presented to the Faculty of the Graduate School of Bioengineering

The University of Texas at Arlington in Partial Fulfillment

of the Requirements

for the Degree of

MASTER OF SCIENCE IN BIOMEDICAL ENGINEERING

THE UNIVERSITY OF TEXAS AT ARLINGTON

May 2015

Acknowledgements

I am grateful to Dr. Jung-Chih Chiao, my advisor and mentor, for granting me the opportunity to work as a member of his research group. His knowledge and ingenuity have been instrumental to driving projects forward, and his guidance provided the motivation for me to continue working. I am also thankful for the financial assistance he provided to me over the duration of my graduate studies.

I would like to thank Dr. Smitha Rao for her guidance and suggestions over the course of my graduate career at the University of Texas at Arlington. Her advice and deep understanding of the principles of my work enabled me to overcome numerous hurdles in experimental design. Under her direction, I expanded my working knowledge of various computational and biological techniques.

I am also grateful to Dr. Victor Lin for his mentorship and guidance. His expertise in the field of cellular and molecular biology granted vital insights into understanding the fundamental mechanisms that drive cellular processes. His scientific knowledge was also critical to the conception and development of experiments.

I am thankful to Dr. Kytai Nguyen and Dr. Cheng-Jen Chuong for their interest in my research and for agreeing to serve as members of my thesis committee.

I would also like to thank my friends and colleagues Steven Bean, Sylvia Loh, Mouhamed Nashawi, Krishna Pabba, Akash Sharma, Omar Johnson, Lindsay Lehman, Jeffrey Mays, Cecile Nguyen, and Ansley Sharna for their assistance with experiments. I would also like to thank the other members of the iMEMS group for their companionship, support, and advice.

To my father, Dr. Wei-Jen Lee, and my mother, Wan-Li Hu, I express my deepest gratitude for their love and unconditional support.

April 16, 2015

Abstract

CHARACTERIZATION AND APPLICATION OF MICROFLUIDIC DEVICES FOR STUDYING CELLULAR MIGRATION AND CHEMOTAXIS

Lyndon K. Lee, MS

The University of Texas at Arlington, 2015

Supervising Professor: Jung-Chih Chiao

Microfluidic devices, often called “lab on a chip”, have been utilized in the fields of physics, chemistry, and biology. In this thesis, the application of a microfluidic device as an *in vitro* assay to study cellular responses to biochemical and biophysical stimuli with a particular focus on the migration and invasion of cancer cells is discussed. The device consists of an array of well pairs joined by 10 microchannels. With device miniaturization and efficient use of space, a large number of experiments can therefore be performed simultaneously on a single platform. Polydimethylsiloxane (PDMS), an optically transparent silicone rubber, was used to fabricate the device and permitted direct visualization of cellular dynamics during migration with the aid of a phase contrast inverted microscope. Using finite element analysis, gradient formation simulations were conducted and showed that chemical gradients could be rapidly generated in zero-flow conditions and remained stable for several days without additional maintenance. This approach allowed for comparatively rapid and simple device analysis without the need for lengthy and resource-intensive fabrication processes. Several microchannel configurations were modeled to examine the steady-state gradient profile, and it was found that linear and nonlinear concentration gradients could be passively generated and maintained for extended durations.

The utility of the device as a platform for studying chemotaxis was demonstrated using several different cell lines. Lung and breast carcinoma cells were found to migrate rapidly through the microchannels of the device towards a gradient of epidermal growth factor, a potent chemoattractant. Prostate cancer cells were exposed to gradients of soluble factors present in various organs, and it was found that the cells migrated preferentially to bone, brain, and testes lysates, Immunocytochemical analysis revealed that cells that entered the channels exhibited upregulation of vimentin, a mesenchymal marker. The role of the novel gene Migration and Invasion Enhancer 1 (MIEN1) in promoting cell migration in breast cancer was also investigated. Overexpression of MIEN1 was associated with increased migration. It was also found that phosphorylation of the canonical immunoreceptor tyrosine-based activation motif (ITAM) is critical to the function of MIEN1. The possible role of MIEN1 in mediating collective migration through the promotion of cell-cell adhesion was also investigated, and although MIEN1-overexpressing cells displayed an increased tendency to form aggregates, immunostaining for several classic cell-cell adhesion molecules revealed no difference between the two conditions. With this platform, multiple cell lines and experimental conditions can be implemented and monitored simultaneously. The microfluidic device can be used to study both chemotaxis and innate migratory potential of adherent cells. Furthermore, *in situ* molecular interrogation of cells by means of immunocytochemistry is demonstrated. With minimal modifications, this platform could be used to study a variety of cell migration-based phenomena.

Table of Contents

Acknowledgements iii

Abstract iv

List of Illustrations ix

List of Tables xii

Chapter 1 Introduction 1

1.1 Introduction 1

1.2 Motivation 2

1.3 Specific Aims 3

1.4 Thesis Organization 3

Chapter 2 Fabrication and Characterization of the Microfluidic Platform 4

2.1 Introduction 4

2.2 Device Design and Fabrication 5

2.2.1 Device Design 5

2.2.2 Photolithographic Template Fabrication 6

2.2.3 Soft Lithography Device Fabrication 6

2.3 Finite Element Analysis Modeling 9

2.3.1 Previous Characterization Attempts 9

2.3.2 Thermal Analogy of Mass Transport 10

2.3.3 Model Development 10

2.3.4 Modeling Near-Complete Channel Occlusion 14

2.3.5 Modeling Alternative Channel Configurations 16

Chapter 3 Cellular Chemotaxis in Response to Gradients of Soluble Factors 20

3.1 Introduction 20

3.2 Chemotaxis to Epidermal Growth Factor 21

3.2.1 Cell Culture 21
3.2.2 Cell Seeding 22
3.2.3 Image Acquisition and Analysis 23
3.2.4 Results and Discussion 23
3.3 Chemotaxis to Organ Lysates 26
3.3.1 Lysate Preparation 26
3.3.2 Cell Culture 27
3.3.3 Cell Seeding 27
3.3.4 Image Acquisition and Analysis 28
3.3.5 Immunocytochemistry 29
3.3.6 Results and Discussion 30
Chapter 4 Cellular Migration and Invasion 37
4.1 Introduction 37
4.2 MIEN1 Localization in MDA-MB 231 38
4.2.1 Cell Culture 38
4.2.2 Immunocytochemistry 38
4.2.3 Results and Discussion 38
4.3 MIEN1 Knockdown 39
4.3.1 Cell Culture 39
4.3.2 siRNA Transfection 39
4.3.3 Cell Seeding 40
4.3.3 Image Acquisition and Analysis 41
Results and Discussion 42
4.4 Influence of MIEN1 Overexpression on Cell Migration 42
4.4.1 Plasmid Construction 42

4.4.2 Cell Transfection and Culture 43
4.4.3 Cell Seeding 44
4.4.4 Image Acquisition and Analysis 45
4.4.5 Results and Discussion 46
4.5 MIEN1 and Cell-Cell Adhesion 51
4.5.1 Cell Culture 51
4.5.2 Hanging Drop Assay 51
4.5.3 Immunocytochemistry 51
4.5.4 Results and Discussion 52
Chapter 5 Conclusions and Future Work 58
Appendix A Additional Experiments and Procedures 61
Appendix B Miscellaneous Code 67
References 74
Biographical Information 82

List of Illustrations

Figure 2-1 Microfluidic device mounted on a tissue culture dish (left) and schematic representation of a well pair with migrating cells (right). 9
Figure 2-2 Geometric model of a well pair in ANSYS 11
Figure 2-3 Color-coded diffusion gradient of EGF across the microchannels 12
Figure 2-4 Plot of the gradient profile across the microchannels at different time points. 12
Figure 2-5 Plot of the gradient profile in a well pair joined by a single microchannel 13
Figure 2-6 Meshed geometric model of a channel with a near-complete occlusion 15
Figure 2-7 Gradient profile across a channel with near-complete occlusion 16
Figure 2-8 Meshed geometric model of a 600 μm-length abruptly tapering channel with a maximum width of 20 μm and a minimum width of 10 μm 17
Figure 2-9 Gradient profile across an abruptly tapering channel 18
Figure 2-10 Meshed geometric model of a continuously tapering channel 19
Figure 2-11 Gradient profile across a continuously tapering channel 19
Figure 3-1 Quantification of migration across microfluidic channels in AxioVision 23
Figure 3-2 Migration of A549 to standard growth medium and 75 ng/ml EGF 24
Figure 3-3 Average migration distance of A549 in response to standard growth medium or 75 ng/ml EGF 25
Figure 3-4 Average migration distance of MDA-MB 231 in response to standard growth medium or 75 ng/ml EGF 26
Figure 3-5 Five-day migration data for PC-3 in response to organ lysates 30
Figure 3-6 Three-day migration data for PC-3 in response to organ lysates 31
Figure 3-7 PC-3 migration in response to standard growth medium 32
Figure 3-8 PC-3 migration in response to growth medium containing lung extract 33
Figure 3-9 PC-3 migration in response to growth medium containing liver extract 33

Figure 3-10 PC-3 migration in response to growth medium containing testes extract 34
Figure 3-11 PC-3 migration in response to growth medium containing kidney extract 34
Figure 3-12 PC-3 migration in response to growth medium containing prostate extract.. 35
Figure 3-13 PC-3 migration in response to growth medium containing femur extract 35
Figure 3-14 PC-3 migration in response to growth medium containing brain extract..... 36
Figure 4-1 Cytosolic MIEN1 (red) localization in MDA-MB 231. F-actin (green) and nucleus (blue) are also shown. 39
Figure 4-2 Efficient MIEN1 knockdown at 72 hours post-transfection of MDA-MB 231 ... 40
Figure 4-3 Fourth-day migration of MDA-MB 231 transfected with non-targeting or MIEN1-targeting siRNA..... 42
Figure 4-4 Peptide sequence of MIEN1 constructs at ITAM and prenylation domains 43
Figure 4-5 Western blot confirming expression of GFP-tagged MIEN1 constructs in MDA-MB 231..... 44
Figure 4-6 Representative images of migration of MDA-MB 231 stably expressing GFP, GFP-MIEN1^{WT}, GFP-MIEN1$^{Y39/50F}$, and GFP-MIEN1$^{Y39/50F, \Delta 112-115}$ 47
Figure 4-7 Average migration distance of the four strains of MDA-MB 231 *p < 0.05, **p < 0.01, ***p < 0.001, ****p < 0.0001..... 48
Figure 4-8 Average count of cells in the channels for the four strains of MDA-MB 231 *p < 0.05, **p < 0.01, ***p < 0.001, ****p < 0.0001..... 48
Figure 4-9 Average migration speed of four strains of MDA-MB 231 ****p < 0.0001..... 50
Figure 4-10 Average persistence of four strains of MDA-MB 231 ***p < 0.001, ****p < 0.0001 50
Figure 4-11 Clustering of suspended MDA-MB 231 in the hanging drop assay..... 53
Figure 4-12 Average cluster size of MDA-MB 231 in suspension *p < 0.05, **p < 0.01.. 53

Figure 4-13 Immunofluorescent staining for e-cadherin (red) in four strains of MDA-MB 231 with DAPI (blue) nuclear stain.....54
Figure 4-14 Immunofluorescent staining for n-cadherin (red) in four strains of MDA-MB 231 with DAPI (blue) nuclear stain.....55
Figure 4-15 Immunofluorescent staining of p120-catenin (red) in four strains of MDA-MB 231 with DAPI (blue) nuclear stain.....55
Figure 4-16 Immunofluorescent staining of β-catenin (red) in four strains of MDA-MB 231 with DAPI (blue) nuclear stain.....56
Figure A-1 A549 wound closure with initial seeding of 150,000 cells.....64
Figure A-2 A549 wound closure with initial seeding of 500,000 cells.....65
Figure A-3 Change in wound area as a percentage of the total image field.....66

List of Tables

Table B-1 List of shortcut keys and functions 69

Chapter 1

Introduction

1.1 Introduction

Microfluidic devices have been used in many scientific and engineering disciplines. Numerous passive and active microfluidic components have been developed for a variety of purposes for chemical, biological, and physical analysis[1-24]. The broad range of materials employed for microfluidic platforms includes silicon, glass, paper, and various polymers. Silicon and glass are durable substrates and have been used for a number of biological studies, but the standard manufacturing techniques such as photolithography require substantial time and resource investments that can raise the cost of such devices[25-28]. Paper-based microfluidic devices are becoming increasingly popular as a low-cost point-of-care diagnostic tool. Microfluidic “channels” can be formed in the paper by selective wax impregnation to create hydrophobic boundaries[29, 30]. However, paper is largely opaque to visible light, making optical interrogation of the sample with a microscope difficult. Furthermore, paper microfluidic devices are largely single-use. Polymers can be tailored to have optimal mechanical, optical, chemical, and biological properties. Polydimethylsiloxane (PDMS), a silicone rubber, is especially attractive for use in biological applications. It is optically flexible, optically transparent, cytocompatible, and chemically inert[31-34]. Moreover, PDMS is easy to clean and the standard device fabrication process of soft lithography is simple and highly repeatable[5, 7, 17, 20, 21, 24, 27]. Thus, with respect to studying cell migration and invasion, PDMS is an ideal material. The platform presented in this thesis has been used as a model for the metastasis of cancer.

1.2 Motivation

Metastasis is characterized by the entry of cancer cells into the circulatory system from the primary tumor and subsequent invasion at distant sites to form secondary tumors, and generally contributes to poor prognosis due to the lack of effective treatments options[20, 21, 27]. Roughly 90% of all human cancer deaths involve metastasis, yet despite the significance of this step in carcinogenesis, the mechanisms by which cancer cells escape the solid primary tumor and spread throughout the body are still not completely understood[35-37]. It is believed that cells must first lose their cell-cell adhesion contacts and then navigate through the extracellular matrix towards a blood or lymphatic capillary. Epithelial-to-mesenchymal transition (EMT) is implicated in this process. EMT is a mechanism by which epithelial cells with strong adhesion to surrounding cells acquire a fibroblast-like phenotype with high motility[35-37]. Upregulation of vimentin is a classic hallmark of a mesenchymal cell, and tumors that contain cells with mesenchymal characteristics are typically graded as more advanced[35-37]. However, recent evidence suggests that other modes of migration such as collective migration can mediate tumor invasion and metastasis[35-39]. It is hypothesized that cancer cells can enter the circulatory system due to the leaky vasculature found in the tumor environment. Upon entry into the circulatory system, cancer cells undergo a complex multi-step process involving detachment from the vessel wall, subsequent reattachment at a distant site, and extravasation to form a secondary tumor[40-51]. This process is believed to be partially regulated by soluble factors present in bodily fluids[35-37]. In addition to external factors, altered gene expression can contribute to the development of more invasive cancer phenotypes. Molecular and visual interrogation of migrating cells can give insight into the mechanisms that regulate metastasis. Developing an *in vitro* model of metastasis that mimics microenvironments

within the body could give deeper insights into the processes that facilitate metastasis and could be useful for developing novel therapies to target previously unknown mechanisms.

1.3 Specific Aims

1. Design, fabricate, and characterize microfluidic devices intended for use as a cell migration and invasion assay.
2. Study the behavior of cancer cells in response to various chemical gradients.
3. Examine the role of novel gene MIEN1 expression in promoting cell migration and invasion.

1.4 Thesis Organization

This thesis is organized as follows: Chapter 2 discusses the design, fabrication, and characterization of the microfluidic platform. Gradient formation is simulated using finite element analysis for a variety of channel configurations and conditions, and it is shown that linear and nonlinear gradient profiles can be established in the channels of microfluidic devices. In Chapter 3, the influence of epidermal growth factor (EGF) and organ lysates on cancer cell migration is presented. In the organ lysate experiment, cells were assessed for expression of mesenchymal markers. Chapter 4 focuses on the role of migration and invasion enhancer 1 (MIEN1) on the migratory behavior of breast cancer cells. The function of an immunoreceptor tyrosine-based activation motif present in the peptide sequence of MIEN1 is elucidated. Molecular characterization of the expression of various cell-cell adhesion markers in breast cancer cells is also investigated to determine MIEN1's role in promoting collective migration.

Chapter 2

Fabrication and Characterization of the Microfluidic Platform

2.1 Introduction

Several assays for studying cell migration have been previously developed and used. Transwell assays are a popular method for studying cellular chemotaxis and invasion[52, 53]. Cells can be seeded on top of a membrane that separates two chambers, and a chemoattractant can be loaded into the bottom chamber. Cell migration across the membrane can then be quantified, but this approach permits only end-point analysis cannot enable detailed interrogations of cellular dynamics during migration. Bridge chamber assays such as the Dunn chamber and Zigmond chamber involve a chamber enclosed by a glass coverslip and can be used to directly visualize cell migration *in situ*[54]. These platforms are able to generate chemical concentration gradients between two reservoirs, but these systems are incompatible with standard inverted microscopes and are prone to gradient disruption during handling. Both of these assays typically require large amounts of potentially expensive reagent.

The spheroid assay requires that cells be embedded in a ball of collagen mounted on a tissue culture substrate. Cells can then exit the collagen spheroid into the surrounding environment[55, 56]. The 3D culture of cells can give better insight into how the cells would behave *in vivo*, but cellular dynamics are difficult to visualize inside the collagen sphere. Additionally, chemical gradients are difficult to generate with this approach; cell migration is difficult to quantify; and the experiment is difficult to reproduce due to variability in the size, shape, and density of the collagen spheroids. Another approach for studying cell migration is the scratch wound assay. Briefly, a “wound” is created in a confluent monolayer of cells by drawing a pipette tip across the tissue culture substrate. The cells are then imaged over time to assess the closure of the wound[51, 57,

58]. While this approach can give some information about the migration of cells and permits molecular interrogation of the sample, the migration is difficult to quantify and differences in seeding density and wound size can skew results and hamper repeatability. The procedure employed to quantify scratch wound migration in different cell seeding density conditions is presented in Appendix A. Furthermore, this assay is not suitable for chemotaxis studies due to the inability to form a concentration gradient.

Several microfluidic systems have previously been proposed. These devices have been used for cell migration studies, biochemical analysis, drug screening, biological systems modeling, and single-cell analysis[59]. With respect to cell migration, a wide array of systems has been developed to generate gradients and examine cellular invasion into extracellular matrix gels[1-24]. However, these systems typically require tightly controlled fluid flow to generate a stable chemical gradient[25-28]. In previous devices that rely on diffusion-driven gradient formation, the medium had to be replaced after several hours to maintain the gradient[1, 12, 14, 16, 20, 21, 23, 27]. This increases the amount of reagent required and increases the complexity of the design. This complexity also contributes to the size of the devices; a large footprint limits the number of devices that can be used simultaneously. Furthermore, such devices are often permanently bonded to a glass substrate, meaning that they are not reusable.

2.2 Device Design and Fabrication

2.2.1 Device Design

The device consisted of 32 well pairs, each connected by a series of 10 identical microchannels. The wells were 5 mm in diameter, and the microchannels were 10 μm in height, 20 μm in width, and 1000 μm in length. The spacing between the channels was 20 μm. The platform could be mounted on a standard 100 mm tissue culture dish. The

material used for final device fabrication was polydimethylsiloxane (PDMS), an optically transparent and chemically inert silicone rubber.

The template of the device was produced using standard microfabrication techniques involving a silicon wafer and photoresist patterning. The device was then fabricated from the template using soft lithographical techniques with PDMS.

2.2.2 Photolithographic Template Fabrication

Detailed fabrication of the device template has been previously described[60-63]. Briefly, a 10-μm thick layer of SU-8 negative photoresist was spin-coated onto a silicon wafer. Subsequent standard microfabrication techniques involving drying, baking, UV exposure, photoresist development, and cleaning produced a master template on a silicon wafer that could be used repeatedly to produce microfluidic platforms. The photoresist was patterned to create outlines of the wells and a negative mold of the microchannels.

2.2.3 Soft Lithography Device Fabrication

Unpolymerized PDMS elastomer was vigorously mixed with its curing agent at a volumetric ratio of 10 parts of PDMS elastomer to 1 part of the curing agent. During the mixing process, a large number of air bubbles were formed in the uncured PDMS. This mixture was poured into a glass plate in sufficient quantity to evenly coat the bottom of the glass plate. The wafer was then mounted in the glass plate and was allowed to sink through the uncured PDMS. This step was performed to stabilize the wafer orientation for future use. Mounting the wafer prior to pouring PDMS in the glass plate could result in a tilted wafer due to uneven infiltration of uncured PDMS into the space between the wafer and the glass plate. Additional 10:1 PDMS was added to the glass plate such that the height of the PDMS above the silicon wafer reached approximately 6 mm. The glass plate was placed on a leveled table surface at room temperature for 24 hours to allow the

PDMS to solidify. During this time, the trapped air bubbles rose to the surface of the fluid boundary and subsequently dissipated. The cured PDMS was visually inspected and found to be bubble-free.

An outline of the silicon wafer was traced in the PDMS using a scalpel, and the PDMS covering the wafer was carefully peeled to produce a 6 mm-thick slab of PDMS with well pair outlines connected by microchannels. Additional PDMS could be poured into the newly created hole outlining the wafer to create more devices. The PDMS was sufficiently flexible to avoid accidental device fracture. Superfluous regions of the PDMS slab were removed with a scalpel blade to create a square of PDMS containing 32 well pair outlines with each well pair outline connected by a series of 10 identical microchannels.

A 5-mm diameter tissue corer was used to create the wells in the PDMS by hand. An inverted microscope was used to assist in the precise positioning of the corer. The completed PDMS device was then cleaned in a solution of detergent in DI water for 20 minutes. The device was then thoroughly washed in DI water to remove any detergent residues. Water droplets on the device were removed using a combination of Pasteur pipette vacuum aspiration and passive evaporation. PDMS that has been cured at room temperature can easily accumulate electrostatic charge and attract airborne dust and debris. These particles can block the microchannels and interfere with proper bonding of the PDMS to the culture dish substrate. To address this issue, the device was wrapped in clear adhesive tape. Devices were then transferred to a biosafety cabinet, and the tape was removed. Devices were temporarily mounted in an enclosed, transparent, and dust-free container and inspected under an inverted microscope to confirm that the dust was completely removed.

Devices were then sterilized by submersion in a 70% v/v solution of ethanol in DI water. The devices were removed from the 70% ethanol solution and dried with the assistance of a vacuum Pasteur pipette. Sterile and dry devices were mounted on a standard 100 mm tissue culture dish. An image of the device with a cartoon representation of the well pairs joined by microfluidic channels is shown in Figure 2-1. PDMS forms a strong, leak-free temporary bond with clean and smooth plastic and glass surfaces[64, 65]. Trapped air between the PDMS and the culture dish substrate was removed by the gentle application of pressure via a plastic micropipette tip. The mounted device was then inspected under an inverted microscope to ensure that complete adhesion to the substrate was achieved. The device was then primed by adding 50 µl of the growth medium for the cells of interest to one well of each well pair. The growth medium was allowed to flow across the channels over the span of 24 hours. The growth medium forced the air out of the microchannels. Device priming also allowed for the identification of any leaks between the device and the tissue culture substrate.

Once the device has been confirmed to be leak-free, cells can be seeded into the wells. The optical properties of PDMS permit *in situ* visualization of the cells with a standard inverted microscope. A detailed procedure for cell seeding and handling is presented in later chapters. Once the experiment has been concluded, the PDMS device can be peeled from the culture dish and cleaned with detergent, water, and ethanol. The PDMS does not degrade during this process and retains its surface and bulk properties. Thus, the device can be reused almost indefinitely.

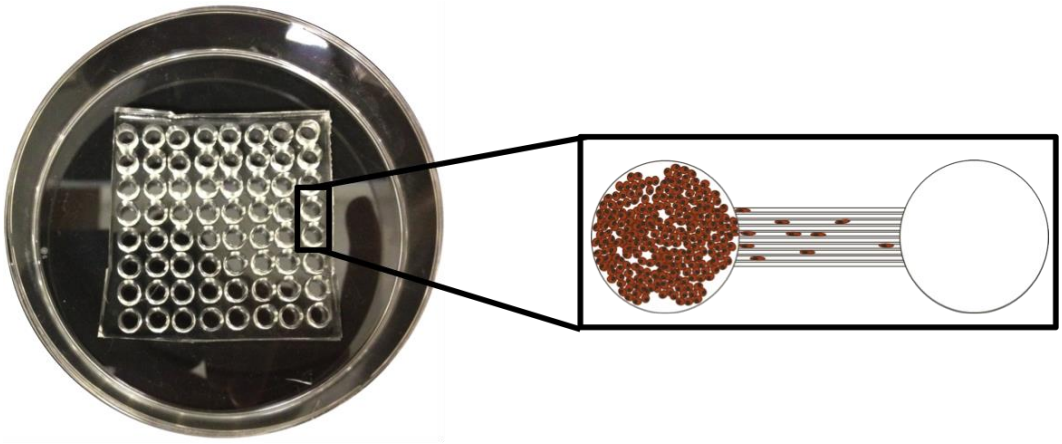

Figure 2-1 Microfluidic device mounted on a tissue culture dish (left) and schematic representation of a well pair with migrating cells (right).

2.3 Finite Element Analysis Modeling

2.3.1 Previous Characterization Attempts

Prior work has been performed to characterize the diffusion and concentration gradient profile formed across the microfluidic channels. Briefly, the device was initially primed, and later, growth medium was added to both wells. The growth medium in one well was then replaced by fluorescein, a water-soluble fluorescent salt[64, 65]. The formation of the gradient was monitored with fluorescence time-lapse microscopy at room temperature at a temporal resolution of 2 minutes per frame. Fluorescence intensity measurements were used to study the formation of the gradient over time. While the results showed the formation of a stable gradient, the steady-state profile was nonlinear. This may have been due to limitations such as inadequate camera sensitivity and light scattering due to the optical properties of PDMS. Furthermore, the study was conducted over the course of only 8 hours and could only be performed after the device had been fabricated. Cell migration experiments typically require several days, meaning that a means of long-term gradient analysis is required, and developing a predictive model for

studying gradient formation could streamline the development of alternative device configurations.

2.3.2 Thermal Analogy of Mass Transport

ANSYS 15.0 was used to model the mass diffusion behavior of a microfluidic device. Since ANSYS does not explicitly support mass transport modeling in zero-flow conditions, a thermal conduction model using transient thermal analysis was used instead. Parallels between thermal conduction and mass diffusion have been previously observed, and the use of thermal conduction to model mass diffusion is well-established in literature[20, 21, 27, 64, 65]. Briefly, dilute mass transport in a zero-flow system can be described by the following equation:

$$\frac{\partial C}{\partial t} = D\nabla^2 C$$

where C represents the concentration a given solute, t represents time, and D represents the diffusivity of a given solute. This is analogous to the equation for thermal conductance:

$$\frac{\partial T}{\partial t} = \frac{k}{\rho C_p}\nabla^2 T$$

where T represents temperature, t represents time, k represents the thermal conductivity of the material, ρ represents the density of the material, and C_p represents the specific heat capacity of the material. Mass diffusivity is equivalent to thermal conductivity when expressed in the same form of units, and density and specific heat capacity can be set to 1 to simplify the equation. From this, it is apparent that concentration and temperature are analogous.

2.3.3 Model Development

A well pair connected by ten identical microchannels of the dimensions described previously was reconstructed in ANSYS, as shown in Figure 2-2.

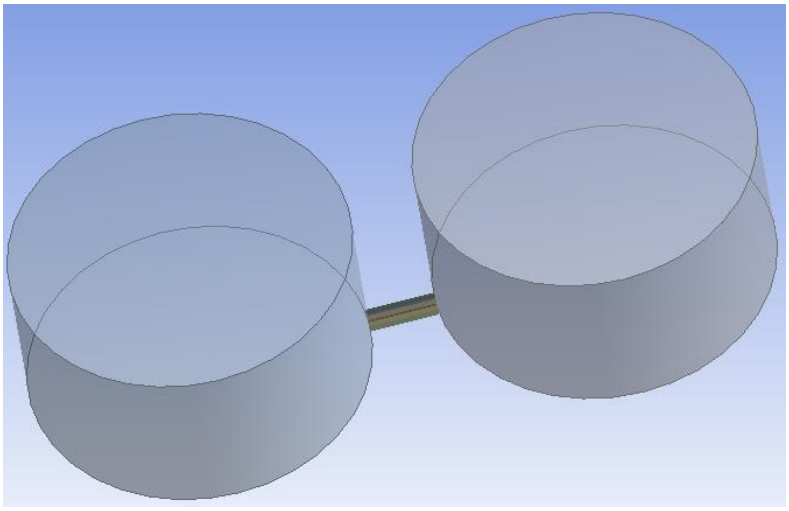

Figure 2-2 Geometric model of a well pair in ANSYS

The fluid height in the wells was calculated from the known fluid volume and the well diameters, and was found to be approximately 2550 μm in height. A mesh was generated, and the outer walls of the wells and channels were insulated in the simulation. The initial temperature in the left well and all channels was set to 0 °C, and the initial temperature in the right well was set to 75 °C to mimic a possible initial concentration distribution of a given chemoattractant in units of ng ml^{-1}. The thermal conductivity of the material used in the model was set to 1.66×10^{-10} W m^{-1} K^{-1}, an analogue to the free diffusion coefficient of epidermal growth factor (EGF), a 6 kDa growth factor that has previously been shown to exert a chemotactic influence on certain cancer cells. It is assumed that EGF does not undergo chemical reactions with any components in the liquid medium and does not adsorb to the surface of the device or tissue culture substrate.

The simulation revealed that a linear gradient was established in less than 50 minutes and could be maintained for over 10 days. A color-coded concentration

distribution across the channels at t = 1×10^{6} sec is presented in Figure 2-3. The data were collected and analyzed in Microsoft Excel, and a concentration vs. distance plot along the top edge of the first channel for multiple time points is presented in Figure 2-4.

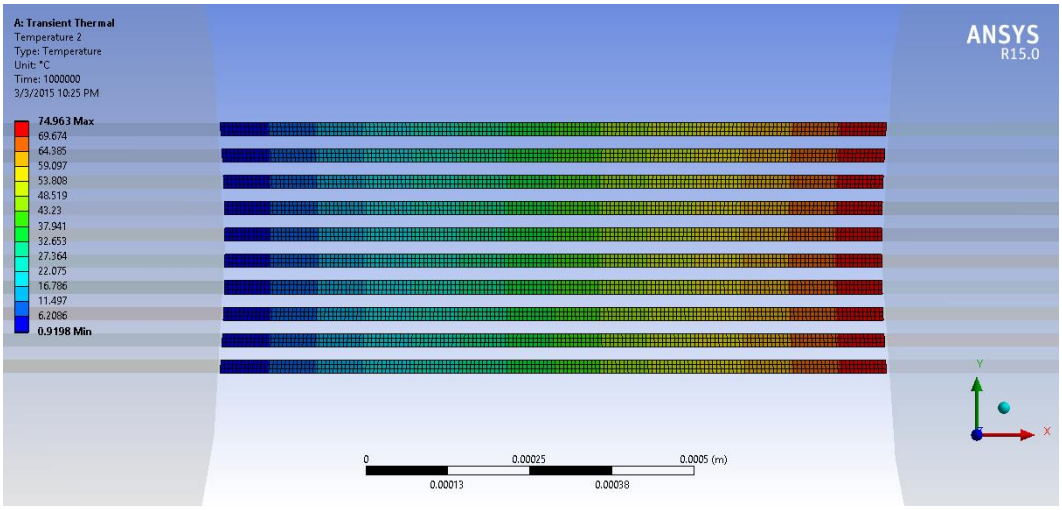

Figure 2-3 Color-coded diffusion gradient of EGF across the microchannels

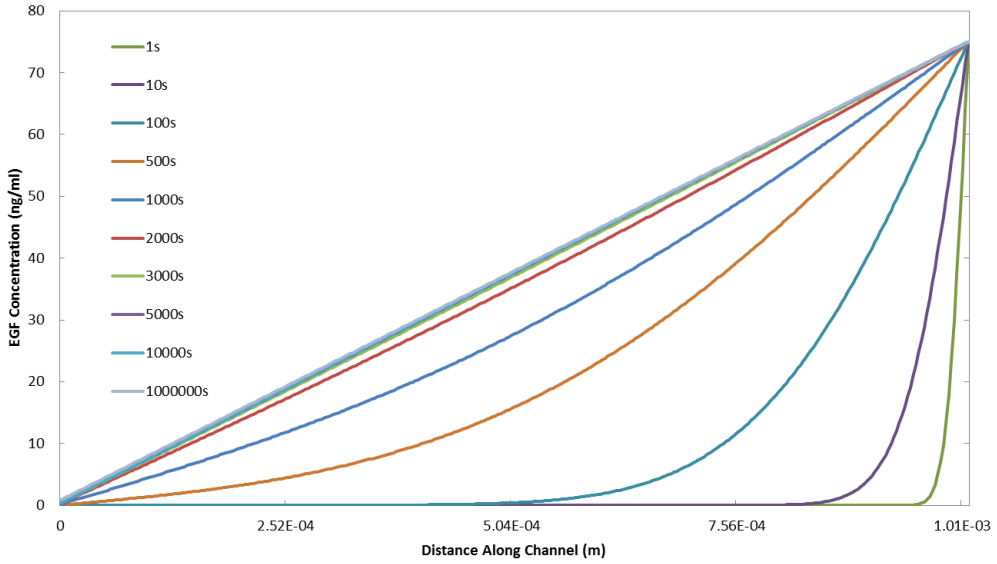

Figure 2-4 Plot of the gradient profile across the microchannels at different time points

In an attempt to further simplify the model geometry, a single-channel device was designed in ANSYS. The single channel was identical to one channel in the 10-channel model. This enabled faster model development and shorter simulation runtimes due to the reduced complexity of the system. The concentration was measured along the centerline of the channel. With the same concentration and diffusion coefficient parameters, a nearly identical diffusion profile was observed, as shown in Figure 2-5. The slight difference in channel length was due to the curvature of the wells.

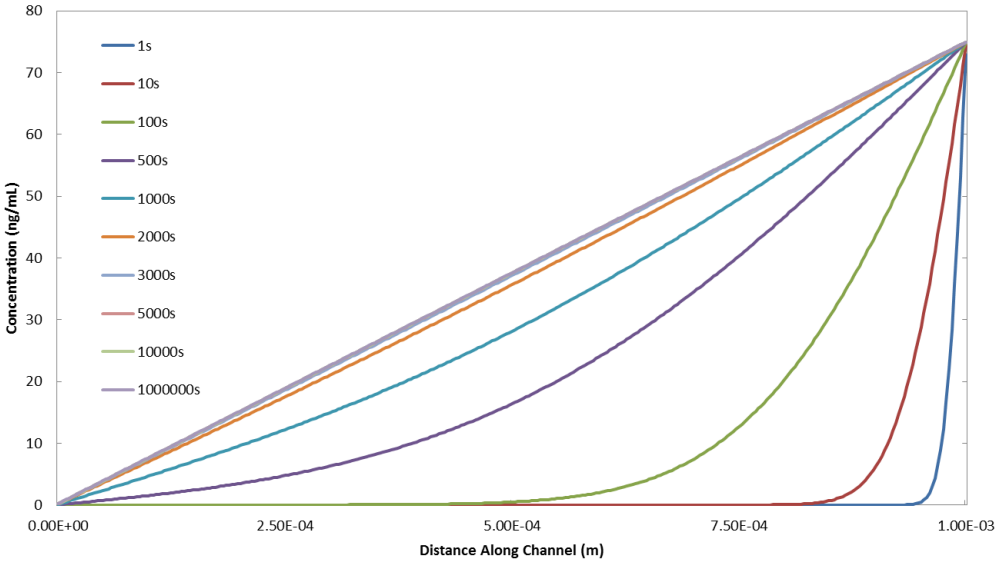

Figure 2-5 Plot of the gradient profile in a well pair joined by a single microchannel

These results indicate that the diffusion profile of a 10-microchannel model can be approximated with high accuracy by a 1-microchannel model for times between 0 seconds and 1×10^6 seconds. Device modeling and simulation with alternative channel configurations can therefore be simplified to a single-channel model with minimal loss of fidelity and significantly reduced time required to perform model construction and computational analysis.

2.3.4 Modeling Near-Complete Channel Occlusion

Near-complete occlusion of the microchannels is a relatively common occurrence when highly migratory cells are studied in the microfluidic device. Thus there is some concern that the obstruction of the channels could interfere with the gradient. A model consisting of two wells joined by a near-completely blocked microchannel was constructed in ANSYS. The shape of the blockage was designed to mimic the morphology of cells migrating through a microchannel. The geometry of the channel is shown in Figure 2-6. The gradient was analyzed using transient thermal analysis. The initial temperature in the left well and the channel was set to 0 °C, and the initial temperature in the right well was set to 75 °C to mimic a possible initial concentration distribution of a given chemoattractant in units of ng ml^{-1}. The thermal conductivity of the material used in the model was set to 1.66×10^{-10} W m^{-1} K^{-1}. Although EGF binds to EGF receptors (EGFR) on the surface of the cell, EGF-EGFR interactions are not modeled in this simplified simulation. Moreover, since cell migration is a relatively slow process, the convective mixing component contributed by moving cells was not considered.

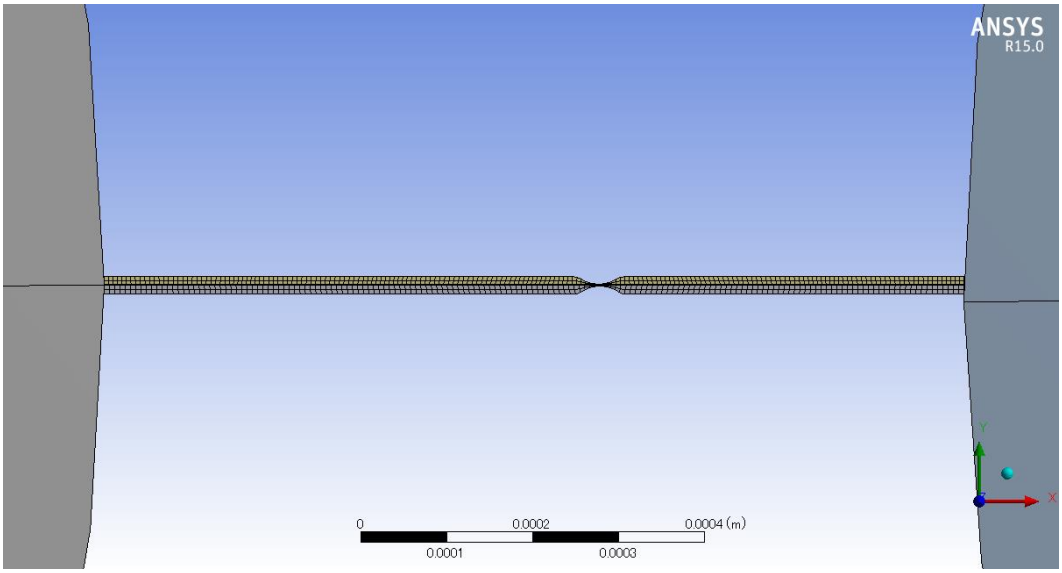

Figure 2-6 Meshed geometric model of a channel with a near-complete occlusion

Figure 2-7 is a plot of the concentration gradient across the channel at multiple time points after the data were collected and plotted in Microsoft Excel. It is clear that the presence of a near-complete occlusion induces a steep concentration gradient at the site of the blockage. Interestingly, since it is believed that the differential binding of factors to different sides of the cells drives cellular chemotaxis, cells may actually travel more quickly under these circumstances. Beyond the blockage, however, a stable linear concentration gradient is rapidly established.

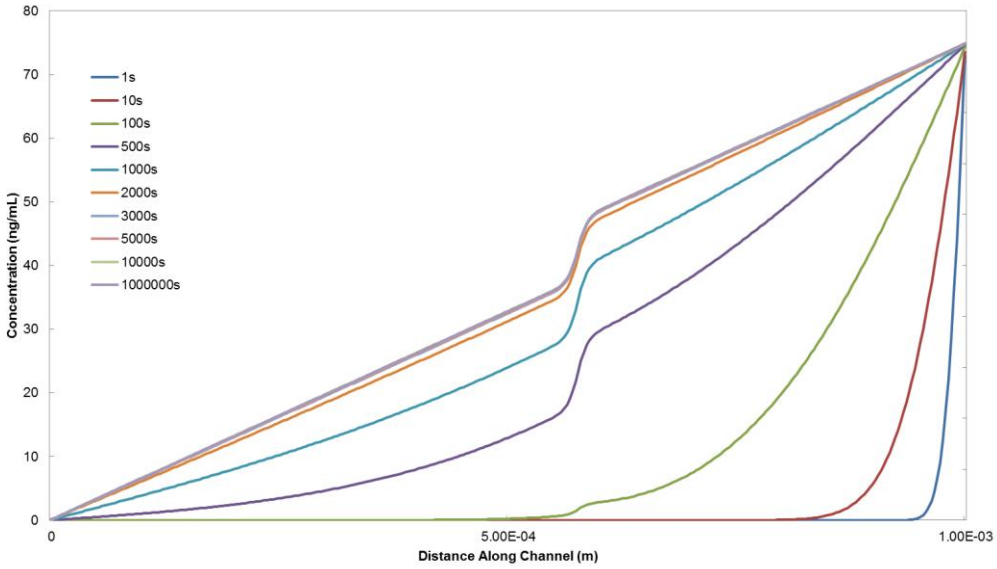

Figure 2-7 Gradient profile across a channel with near-complete occlusion

2.3.5 Modeling Alternative Channel Configurations

There is interest in generating nonlinear gradients in a microfluidic device. Many proposed devices require flow systems and complex channel configurations to achieve this end. Finite element analysis modeling can be used to test different channel configurations to determine optimal gradient profiles. Two types of channels are presented in this section: the abruptly tapering channel and the continuously tapering channel. The diffusion profile of EGF across these channels is investigated using ANSYS transient thermal analysis.

The abruptly tapering channel has been previously described and fabricated[64]. The channel is 600 μm in length and tapers from 20 μm in width to 10 μm in width over the distance of 50 μm. It has been used to study cellular chemotaxis and general behavior when cells are subjected to rigid confinement. However, the steady state concentration gradient profile in the channels has not been characterized. The mesh model of the channel is displayed in Figure 2-8 below.

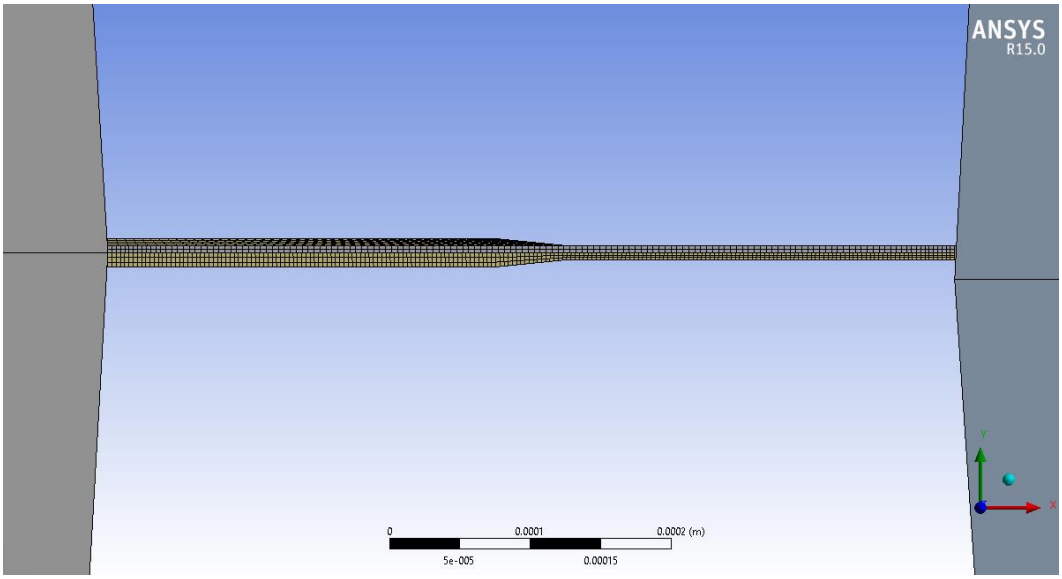

Figure 2-8 Meshed geometric model of a 600 μm-length abruptly tapering channel with a maximum width of 20 μm and a minimum width of 10 μm

A simulation was conducted using the same initial conditions of 0 °C in the left well and channels and 75 °C in the right well. The data were collected and plotted in Microsoft Excel, as shown in Figure 2-9. From the plot, it can be seen that the narrow region of the channel corresponds to a steeper gradient profile. Furthermore, the time required to form a stable gradient is lower, owing to the shorter length of the channel. Thus, if extremely rapid gradient formation is required for an experiment, then shorter channels may be a viable option. The shorter diffusion distance may also decrease the effective lifespan of the gradient, but the simulation results show that the gradient does not change substantially over the course of many days.

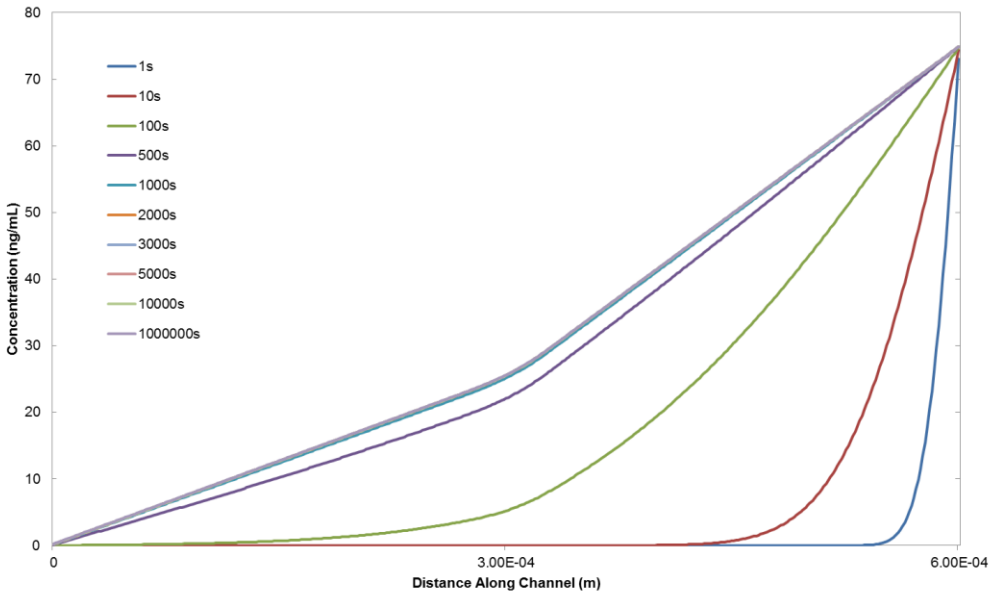

Figure 2-9 Gradient profile across an abruptly tapering channel

A 1000 μm-length microchannel that tapers continuously from 20 μm to 5 μm was also modeled. The meshing and geometry of the channel is shown in Figure 2-10. The simulation results at multiple time points are presented in Figure 2-11. The gradient stabilizes in approximately the same time as other 1000 μm-length microchannel designs. However, the profile is decidedly nonlinear. Much like the abruptly tapering channel, the continuously tapering channel exhibits a steeper gradient profile in the narrower regions.

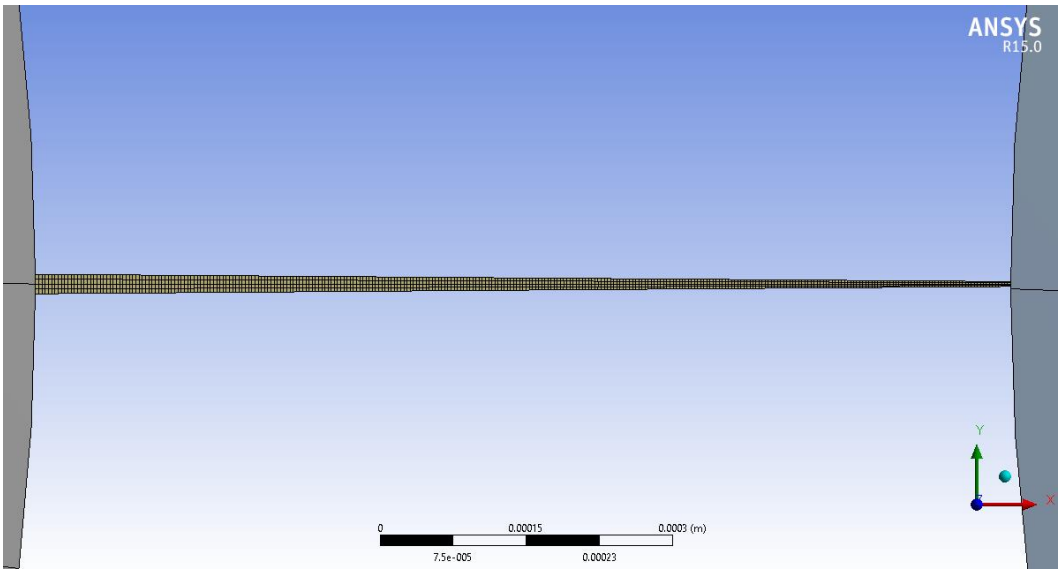

Figure 2-10 Meshed geometric model of a continuously tapering channel

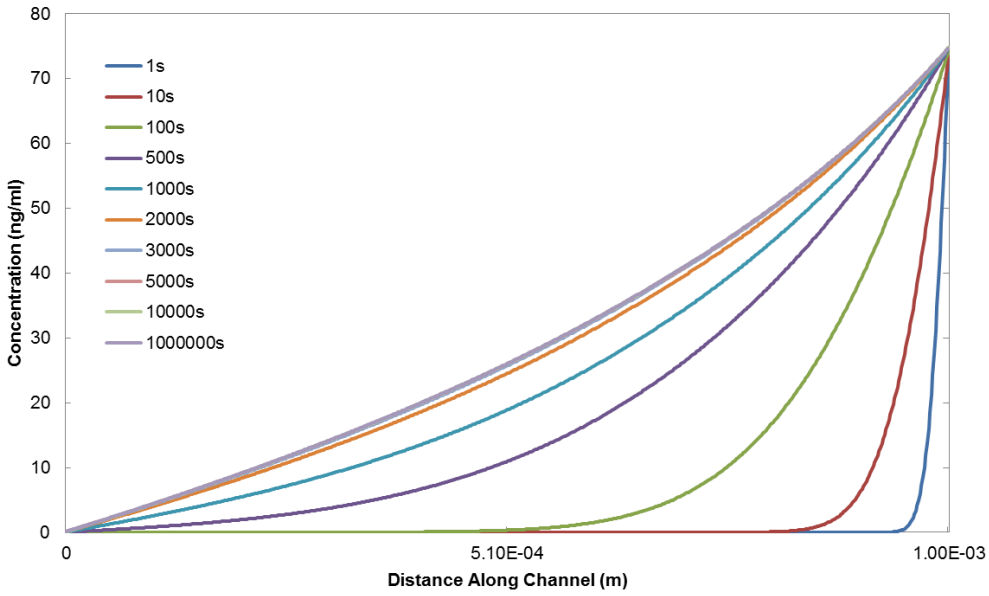

Figure 2-11 Gradient profile across a continuously tapering channel

Chapter 3

Cellular Chemotaxis in Response to Gradients of Soluble Factors

3.1 Introduction

Lung cancer is one of the deadliest and most prevalent cancers in the world. With an abysmal overall 5-year survival rate of only 15%, it kills more people than prostate, breast, and colorectal cancers combined[66]. In the United States alone, more than 200,000 new cases of lung cancer and over 150,000 lung cancer-related deaths are expected each year. Moreover, lung cancer is typically highly aggressive; 70% of all detected cases present locally advanced or metastatic tumors and the 5-year survival even at the earliest stage hovers around 50%[64]. A key receptor commonly overexpressed in lung cancer is epidermal growth factor receptor (EGFR)[67, 68]. Upon binding of ligands such as EGF, EGFR's intracellular domain is phosphorylated which can promote mitogenesis, cytoskeletal rearrangement, and cell survival through a variety of different signaling pathways[67].

Triple negative breast cancer (TNBC) is a class of breast cancer that does not express estrogen receptors, progesterone receptors, or human epidermal growth factor receptor 2, all of which are commonly used markers and therapeutic targets for breast cancer[69, 70]. As a result, TNBC is unresponsive to a variety of treatment options such as Tamoxifen and aromatase inhibitors. Moreover, TNBC tends to be more aggressive, has a greater relapse probability, and has generally poorer outcome than other forms of breast cancer[69, 70]. The lack of distinguishing surface markers makes this form of breast cancer particularly difficult to target for drug delivery. Like lung cancer, TBNC and many other breast cancers tend to overexpress EGFR[71].

Previously, it has been shown that EGF concentration gradients exert a chemotactic effect on many different types of cancers[71]. The first set of experiments

presented in this chapter attempts to both confirm these findings and validate the microfluidic platform as a robust means of assessing cellular migration and chemotaxis.

The second part of this chapter focuses on the migration of prostate cancer towards dilute solutions containing organ extract proteins. Prostate cancer is the second most prevalent cancer and second greatest cause of cancer-related death among men[71, 72]. One in seven men is expected to develop prostate cancer in their lifetime[23, 62, 64]. Typical 5-year survival rates for non-metastatic cases are nearly 100%, but this value drops significantly in the event of metastasis—only 28% of patients with metastases survive for longer than 5 years. An overwhelming majority of metastatic prostate cancers form secondary tumors in the bone[73]. While physical characteristics such as vascular structure likely play a role in this organ-specific migration, it is believed that soluble factors produced by tissues exert a chemotactic effect on these cancer cells. This work examines the behavior of prostate cancer cells in response to organ extract concentration gradients using a microfluidic device. Gene expression profiling is also conducted to determine whether different organ extracts can induce differential gene expression to facilitate the development of more invasive cancer cell phenotypes.

3.2 Chemotaxis to Epidermal Growth Factor

3.2.1 Cell Culture

Human lung adenocarcinoma cell line A549 was cultured in RPMI 1640 supplemented with 10% fetal bovine serum (FBS), 100 U/ml penicillin, and 100 µg/ml streptomycin. Human breast carcinoma cell line MDA-MB 231 was cultured in low glucose Dulbecco's Modified Eagle Medium (DMEM) supplemented with 10% FBS, 100 U/ml penicillin, and 100 µg/ml streptomycin. Human breast normal epithelium cell line MCF 10A was cultured in MEGM serum-free growth medium supplemented with 100 ng/ml cholera enterotoxin, 100 U/ml penicillin, and 100 µg/ml streptomycin. The MEGM

kit includes gentamicin, but this was not included in the final growth medium preparation. Cells were grown in 100 mm tissue culture dishes to approximately 70% confluence. Cells were incubated at 37 °C in 5% CO_2 and 95% standard atmosphere.

3.2.2 Cell Seeding

The cell growth medium was aspirated, and the cells were rinsed in sterile phosphate-buffered saline (PBS). The PBS was aspirated, and 500 µl 0.25% trypsin EDTA was added to the cells. The cells were stored in the incubator for 5 minutes. Cellular detachment from the tissue culture substrate was confirmed with the aid of an inverted microscope. The cells were then suspended in 1 ml of FBS-supplemented growth medium to neutralize the trypsin. The cells suspension was transferred to a 15-ml conical vial and was centrifuged at 3500 rpm for 3 minutes. The liquid supernatant was aspirated from the conical vial to leave only the cell pellet. The pellet was resuspended in 1 ml of growth medium. With the aid of a micropipette, 15 µl of the suspension was pipetted into a vial, and 15 µl of 0.4% trypan blue solution was added to the same vial and mixed. A hemocytometer was used to quantify the concentration of the cell suspension.

The stock cell suspension was diluted to create a working cell suspension with a concentration of 6×10^4 cells/ml. The priming growth medium was removed from a cleaned and primed device, and 50 µl of the diluted cell suspension was added to the left well in each well pair to achieve a seeding density of 3×10^3 cells/well. Standard growth medium containing either 75 ng/ml EGF or no additional factors was added to the right well in each well pair. For each cell line and chemoattractant condition, a total of 16 well pairs were used. The areas of the tissue culture dish that were not covered by the PDMS device were filled with sterile PBS to limit the evaporation of growth medium from the wells. The growth medium was replaced every 48 hours in all wells.

3.2.3 Image Acquisition and Analysis

Brightfield images of the cells within the channels were captured at 100× magnification at 24 hour intervals with a Ti Eclipse Nikon microscope for 72 hours. These images were analyzed using AxioVision (Zeiss, USA) to determine the position of the leading cell in each channel relative to the leftmost point of each channel. Channels containing no cells were assigned a value less than 10 μm. An example is shown in Figure 3-1 below. The migration distance data were subsequently organized by day and experimental condition with a MATLAB program, which also converted measurement values lower than 10 μm to 0 μm. The results were written to a Microsoft Excel spreadsheet for further analysis.

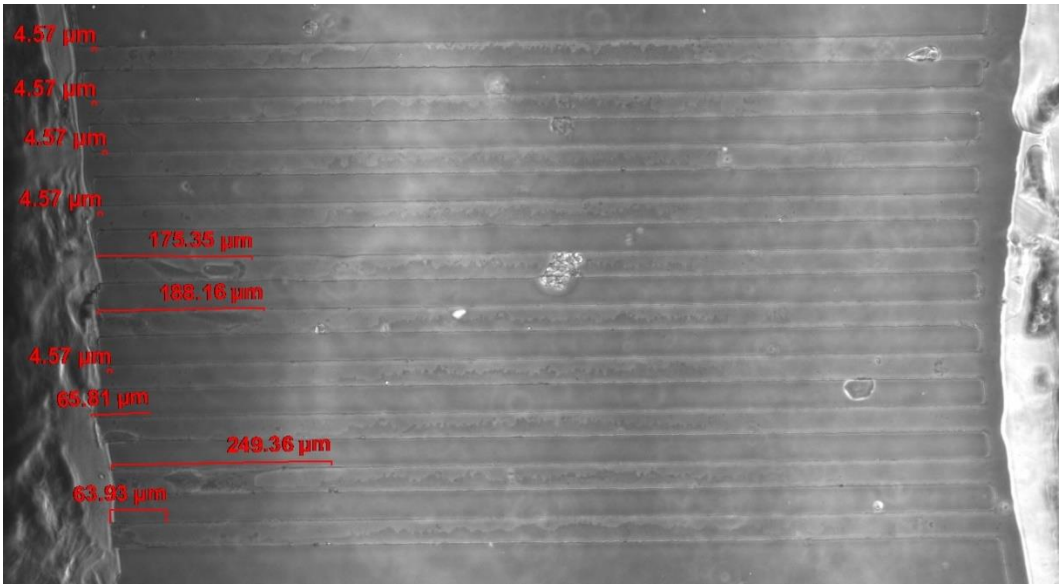

Figure 3-1 Quantification of migration across microfluidic channels in AxioVision

3.2.4 Results and Discussion

A549 was found to exhibit significantly increased migration in response to a gradient of EGF. Images representative of the typical response of A549 to the two

conditions over the course of 72 hours are presented in Figure 3-2 below. The cells were colored in post-processing to allow for better visibility.

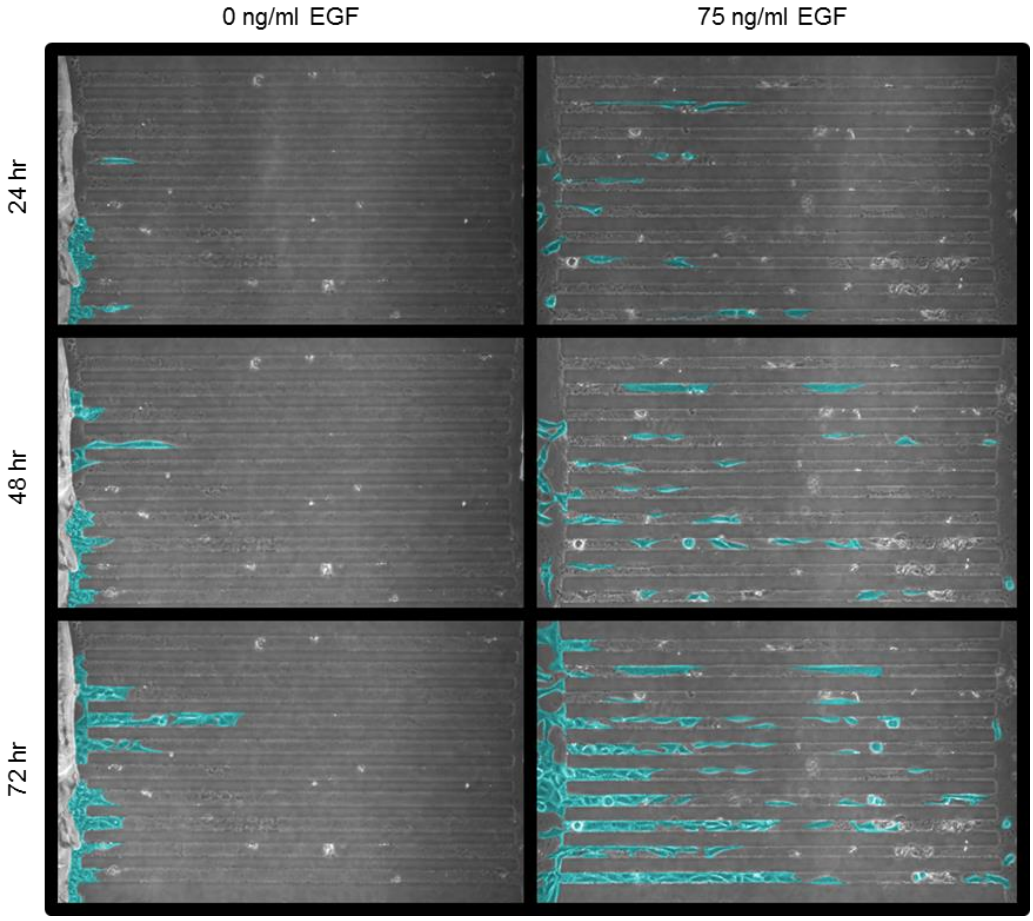

Figure 3-2 Migration of A549 to standard growth medium and 75 ng/ml EGF

The migration data for A549 were aggregated into a Microsoft Excel spreadsheet, and a plot was generated as seen in Figure 3-3. A Student's t-test was performed, and the average migration distance of A549 in response to an EGF concentration gradient was found to be significantly higher than the migration distance of A549 in response to no concentration gradient on all days ($p < 0.01$).

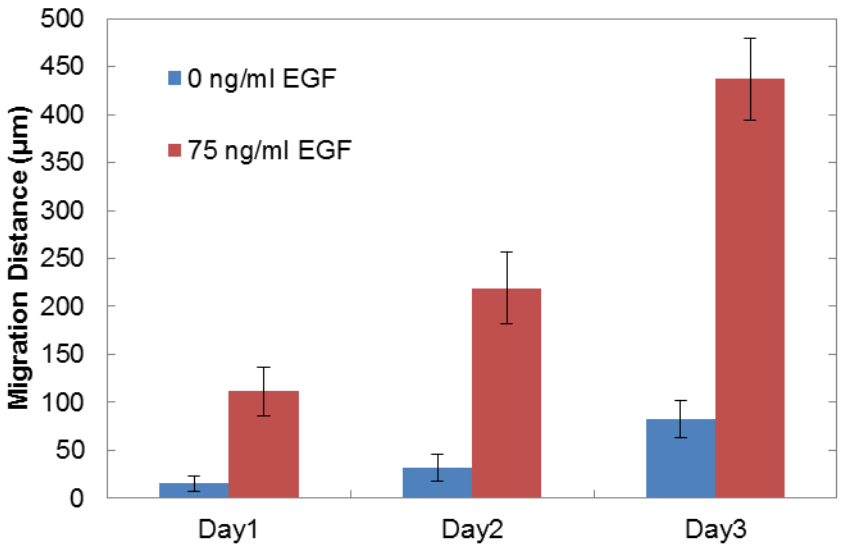

Figure 3-3 Average migration distance of A549 in response to standard growth medium or 75 ng/ml EGF

Similarly, MDA-MB 231 was found to exhibit significantly increased migration in response to a gradient of EGF. The migration data for MDA-MB 231 were aggregated into a Microsoft Excel spreadsheet, and a plot was generated as seen in Figure 3-4. A Student's t-test was performed, and the average migration distance of MDA-MB 231 in response to an EGF concentration gradient was found to be significantly higher than the migration distance of MDA-MB 231 in response to no concentration gradient on the second and third days ($p < 0.05$).

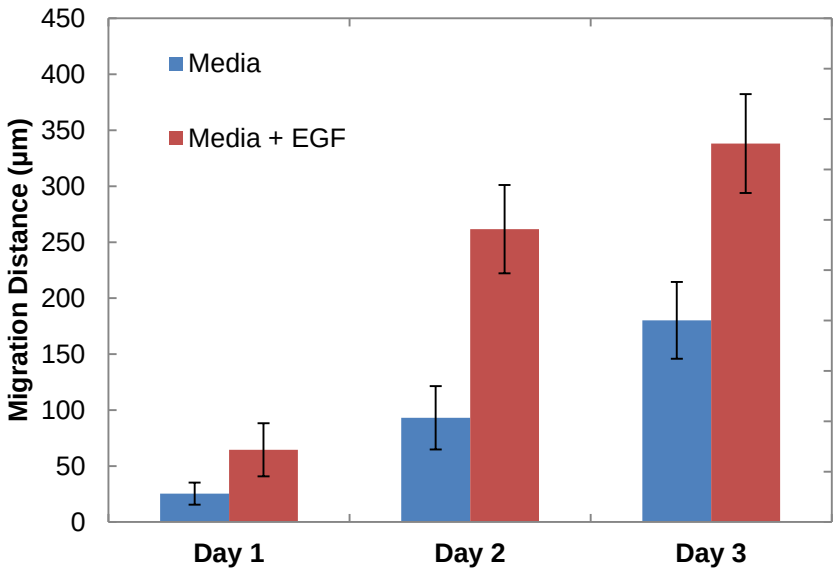

Figure 3-4 Average migration distance of MDA-MB 231 in response to standard growth medium or 75 ng/ml EGF

No migration was observed in MCF 10A. The cells proliferated and survived over the course of the allotted 72 hours, but failed to enter the channels.

These data coupled with previously established results demonstrates the functional significance of EGF in cellular migration and the utility of the microfluidic device for studying cellular chemotaxis. This highlights the potential applications of this device as a means for studying the influence of signaling molecules on cancer cell behavior.

3.3 Chemotaxis to Organ Lysates

3.3.1 Lysate Preparation

Lungs, livers, testes, kidneys, prostates, femurs, and brains were extracted from adult male Sprague-Dawley rats. The organs were frozen at -80 °C for long-term storage. The organs were further cooled in liquid nitrogen to make them more susceptible to pulverization and were powdered with a tissue pulverizer consisting of a steel chamber to hold an organ and a hammer-driven steel piston. The powdered and frozen organs were

transferred to individual vials containing tissue extraction buffer consisting of 0.05 M Tris-HCl (pH 7.4), 0.5 M sodium chloride, 5 mM N-ethylmaleimide, 5 mM EDTA, 1 mM phenylmethylsulfonylfluoride, gentamicin (50 mg/ml), and a protease inhibitor cocktail. The protease inhibitor helps to prevent proteolytic degradation of the proteins in the organ lysate samples. The organ samples were then placed on a rocker and were gently agitated overnight in ice.

The liquid fractions of the organ samples were transferred to centrifuge tubes containing a 0.22-µm filter. The liquid fractions were then centrifuged at 13000 rpm for 10 minutes to remove any suspended particulate matter and to sterilize the organ lysates. The fraction that passed through the filter was twice dialyzed against RPMI 1640 for 24 hours. The organ lysates were aliquoted into cryogenic vials and stored at -80 °C to limit protein degradation. The protein concentrations of the various organ lysates were measured using a Bradford total protein assay. Organ lysates were then diluted in growth medium to achieve a total organ protein concentration of 8 µg/ml.

3.3.2 Cell Culture

Human prostate carcinoma cell line PC-3 was cultured in RPMI 1640 supplemented with 10% fetal bovine serum (FBS), 100 U/ml penicillin, and 100 µg/ml streptomycin. Human normal prostate epithelium cell line PZ-HPV-7 was grown in PrEGM serum-free medium supplemented with 100 U/ml penicillin, and 100 µg/ml streptomycin. Cells were grown in 100 mm tissue culture dishes to approximately 70% confluence. Cells were incubated at 37 °C in 5% CO_2 and 95% standard atmosphere.

3.3.3 Cell Seeding

The cell growth medium was aspirated, and the cells were rinsed in sterile phosphate-buffered saline (PBS). The PBS was aspirated, and 500 µl 0.25% trypsin EDTA was added to the cells. The cells were stored in the incubator for 5 minutes.

Cellular detachment from the tissue culture substrate was confirmed with the aid of an inverted microscope. The cells were then suspended in 1 ml of FBS-supplemented growth medium to neutralize the trypsin. The cells suspension was transferred to a 15-ml conical vial and was centrifuged at 3500 rpm for 3 minutes. The liquid supernatant was aspirated from the conical vial to leave only the cell pellet. The pellet was resuspended in 1 ml of growth medium. With the aid of a micropipette, 15 µl of the suspension was pipetted into a vial, and 15 µl of 0.4% trypan blue solution was added to the same vial and mixed. A hemocytometer was used to quantify the concentration of the cell suspension.

The stock cell suspension was diluted to create a working cell suspension with a concentration of 1×10^5 cells/ml. The priming growth medium was removed from a cleaned and primed device, and 50 µl of the diluted cell suspension was added to the left well in each well pair to achieve a seeding density of 5×10^3 cells/well. Standard growth medium supplemented with one of the organ lysates or no additional factors was added to the right well in each well pair. For each cell line and chemoattractant condition, a total of 4 well pairs were used. The areas of the tissue culture dish that were not covered by the PDMS device were filled with sterile PBS to limit the evaporation of growth medium from the wells. The growth medium was replaced every 48 hours in all wells.

3.3.4 Image Acquisition and Analysis

Brightfield images of the cells within the channels were captured at 100× magnification at 24 hour intervals with a Ti Eclipse Nikon microscope for 72 hours. These images were analyzed using AxioVision (Zeiss, USA) to determine the position of the leading cell in each channel relative to the leftmost point of each channel. Channels containing no cells were assigned a value less than 10 µm. The migration distance data were subsequently organized by day and experimental condition with a MATLAB

program, which also converted measurement values lower than 10 μm to 0 μm. The results were written to a Microsoft Excel spreadsheet for further analysis.

3.3.5 Immunocytochemistry

Upon the conclusion of the migration assay, the microfluidic device was carefully peeled from the tissue culture substrate. It has been established that cells do not form strong adhesions to the channel walls and instead preferentially attached to the tissue culture substrate. This allowed the device to be removed with minimal disturbance to the cells. PC-3 cells were then fixed in a solution of 4% paraformaldehyde in PBS for 20 minutes. The paraformaldehyde was removed and the cells were rinsed twice with PBS for 15 minutes per rinse. The cells were then blocked for 1 hour with a PBS solution containing 0.25% Triton X-100, 0.1% bovine serum albumin (BSA), and 10% goat serum. Samples were again rinsed twice with PBS. Cells were then incubated with a PBS solution containing 0.25% Triton X-100, 0.1% BSA, 3% goat serum, and 20 μg/ml anti-vimentin immunoglobulin G (clone V9) overnight at 4 °C. The primary antibody solution was removed and the sample was again rinsed twice with PBS for 15 minutes per rinse to remove any unbound antibodies. The cells were then incubated in a secondary antibody solution consisting of 0.25% Triton X-100, 0.1% BSA, 3% goat serum, and 20 μg/ml fluorescein isothiocyanate (FITC)-labeled goat anti-mouse immunoglobulin G for 2 hours. A 5 ng/mL solution of 4’ 6-diamidino-2-phenylindole (DAPI) dissolved in PBS was used as a nuclear stain. Ultraviolet fluorescence microscopy was employed to visualize vimentin expression and localization within the cells.

3.3.6 Results and Discussion

Migration data over the course of five days were collected. PC-3 cells began migrating in most conditions by the end of the first day. PZ-HPV-7 failed to migrate in any condition over the course of the five-day experiment. The average distance of the leading cell in each condition for each day is presented in Figure 3-5 below.

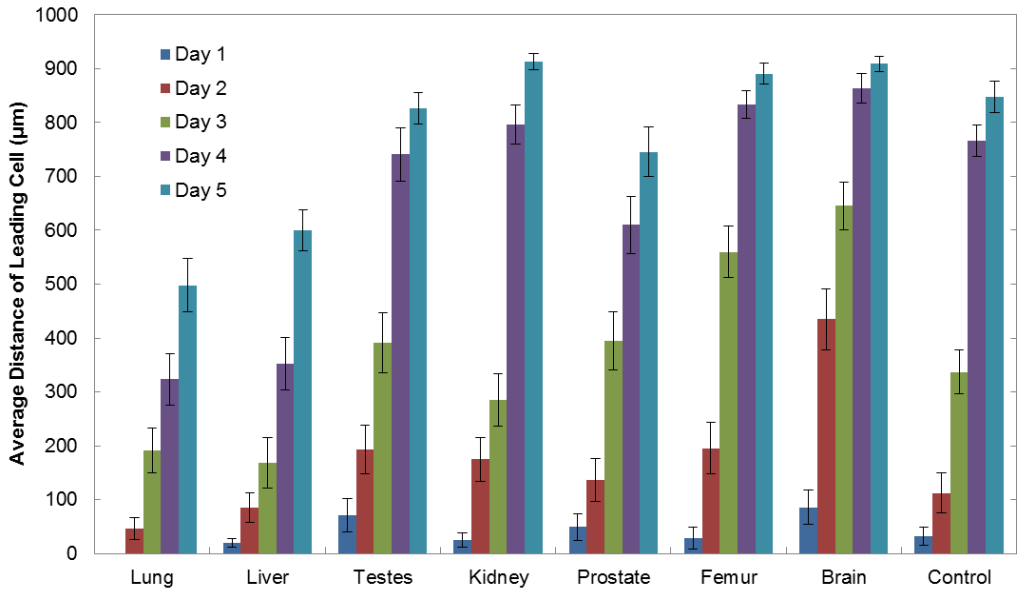

Figure 3-5 Five-day migration data for PC-3 in response to organ lysates

It is apparent that at the later time points, many cells had already traversed the entire length of the microchannels, which explains the apparent saturation of the values on the fourth and fifth days. To mitigate these effects, the migration data for the first three days were examined. The results are presented in Figure 3-6 below.

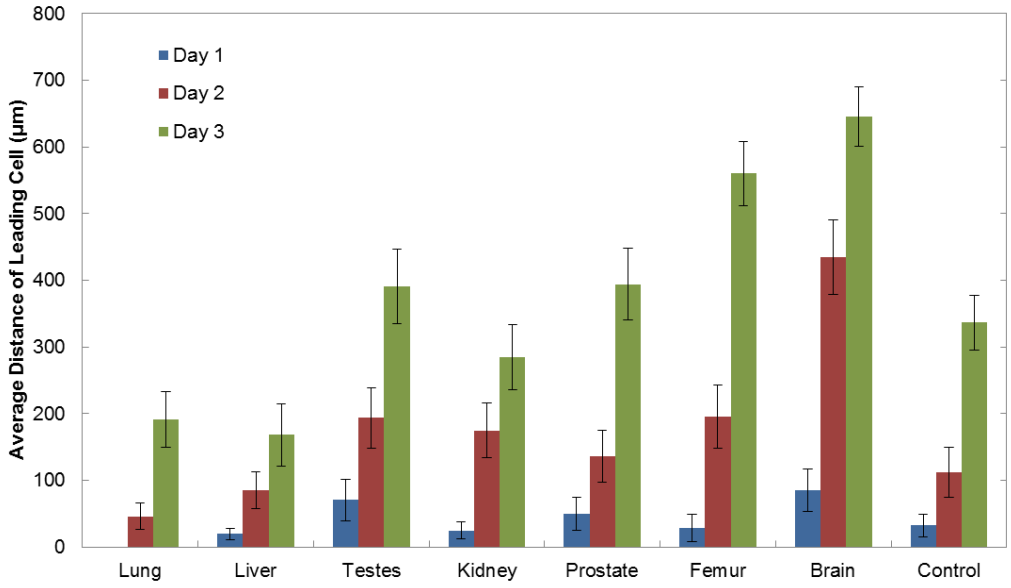

Figure 3-6 Three-day migration data for PC-3 in response to organ lysates

PC-3 was found to migrate significantly greater distances towards femur and brain lysates compared to the control ($p < 0.05$). Conversely, PC-3 exhibited lower migration towards lung and liver lysates ($p < 0.05$). The migration of PC-3 to testes, kidney, and prostate extracts did not differ significantly from the control.

Immunocytochemical analysis revealed that PC-3 expressed appreciable levels vimentin. However, it was also found that migratory cells appeared to fluoresce more brightly, indicating a higher level of vimentin expression. Figure 3-7 shows PC-3 migrating through the channels in the absence of a gradient. From the image, it is clear that PC-3 cells that have entered the channels largely express greater levels of vimentin than their stationary counterparts. It can also be seen that these cells continue to express elevated levels of vimentin upon leaving the channel, as seen in the upper right corner of the image. Similar results were found in the other experimental conditions where PC-3 was exposed to organ lysate concentration gradients, as shown in Figures 3-8 to 3-14. Vimentin is a classic marker for mesenchymal cells, and patients with cancer cells that

have a mesenchymal phenotype tend to have poorer prognoses[73]. These data suggest that even within the same cell line, there exists a subpopulation of cells that have an altered gene expression which may contribute to a more motile and invasive phenotype.

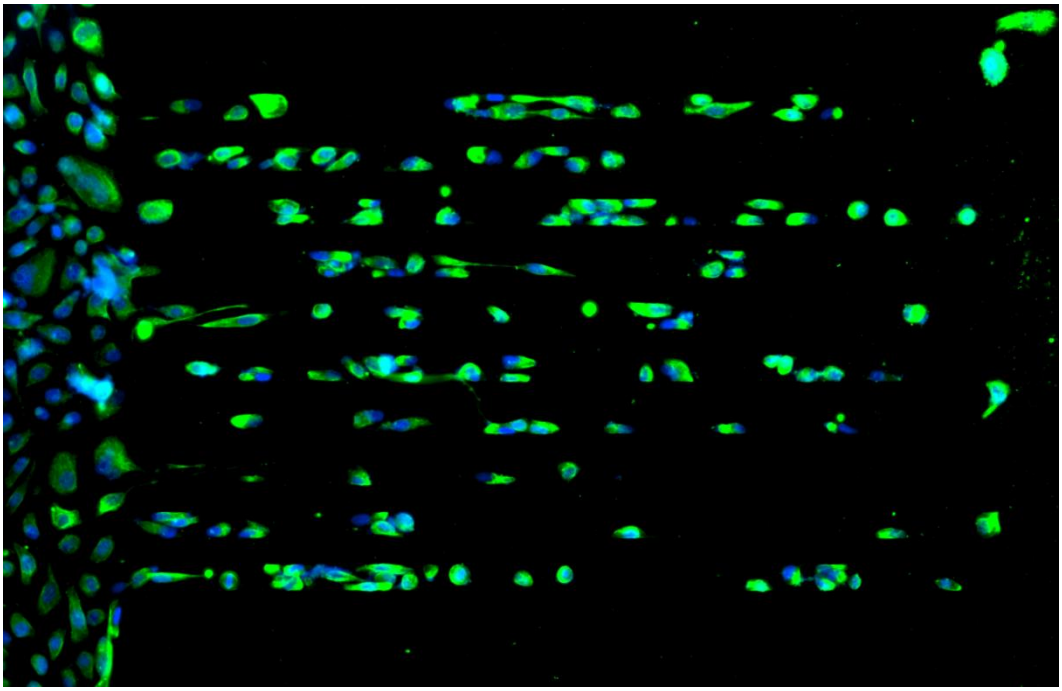

Figure 3-7 PC-3 migration in response to standard growth medium

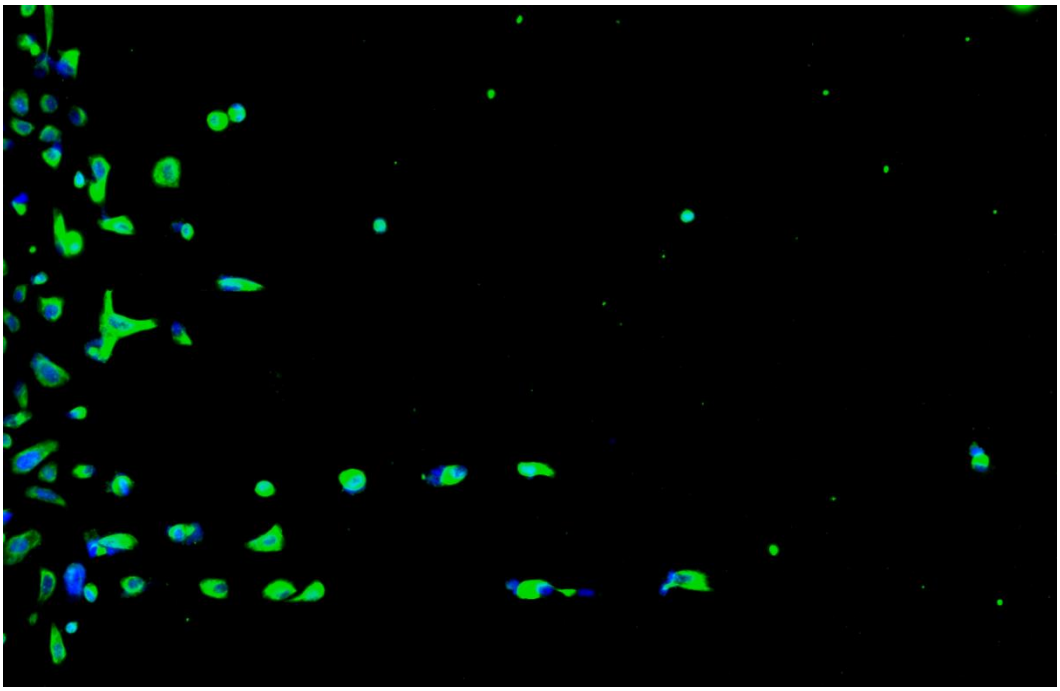

Figure 3-8 PC-3 migration in response to growth medium containing lung extract

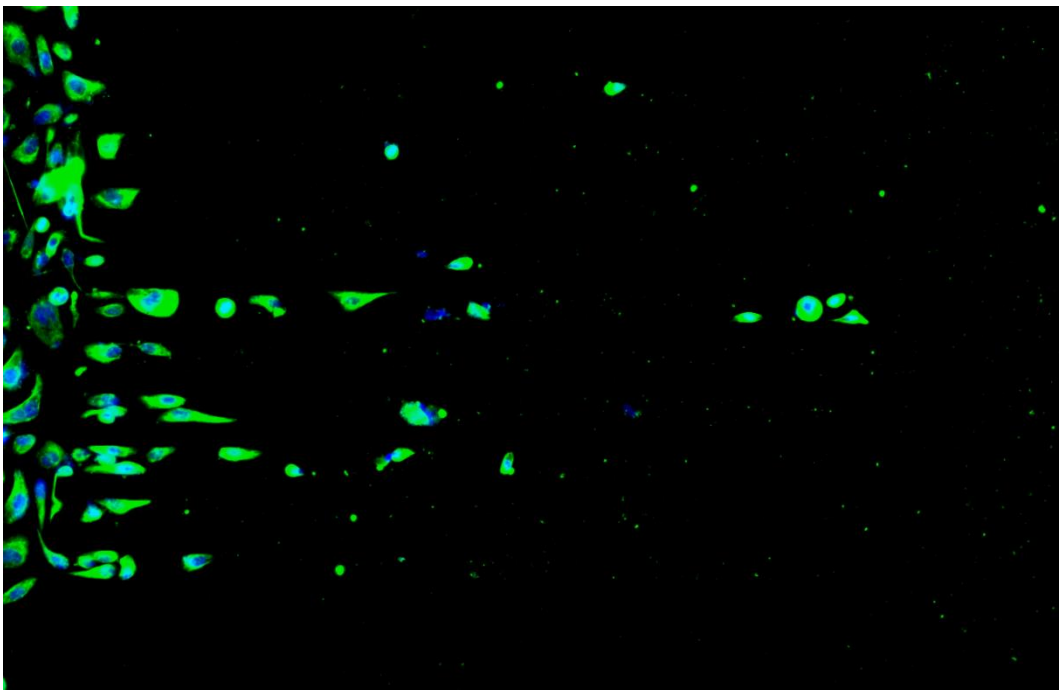

Figure 3-9 PC-3 migration in response to growth medium containing liver extract

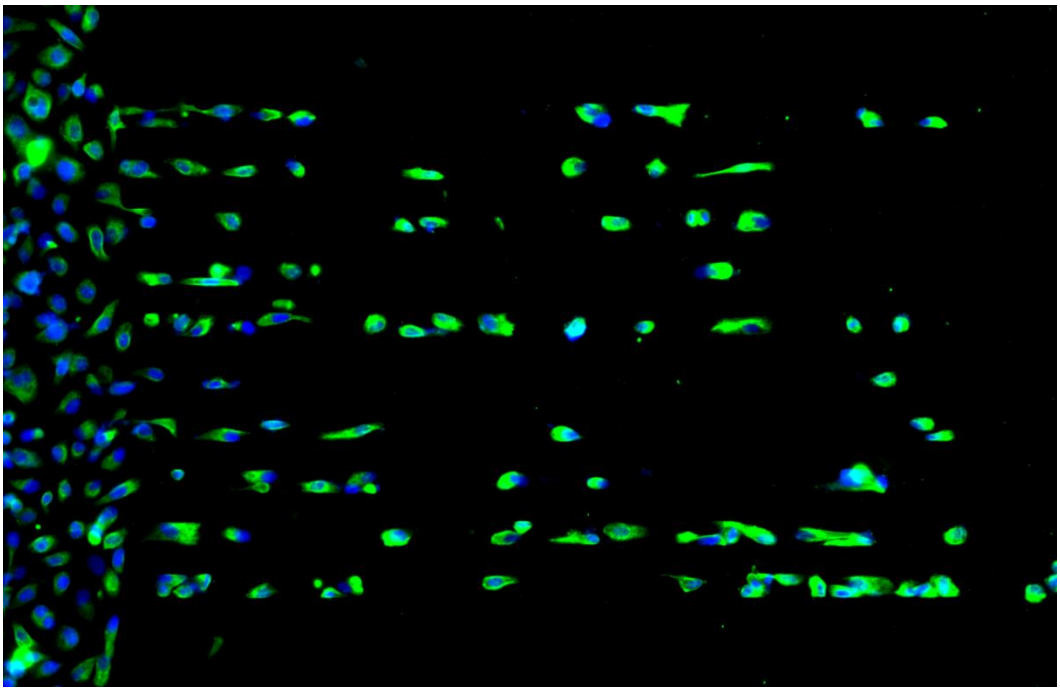

Figure 3-10 PC-3 migration in response to growth medium containing testes extract

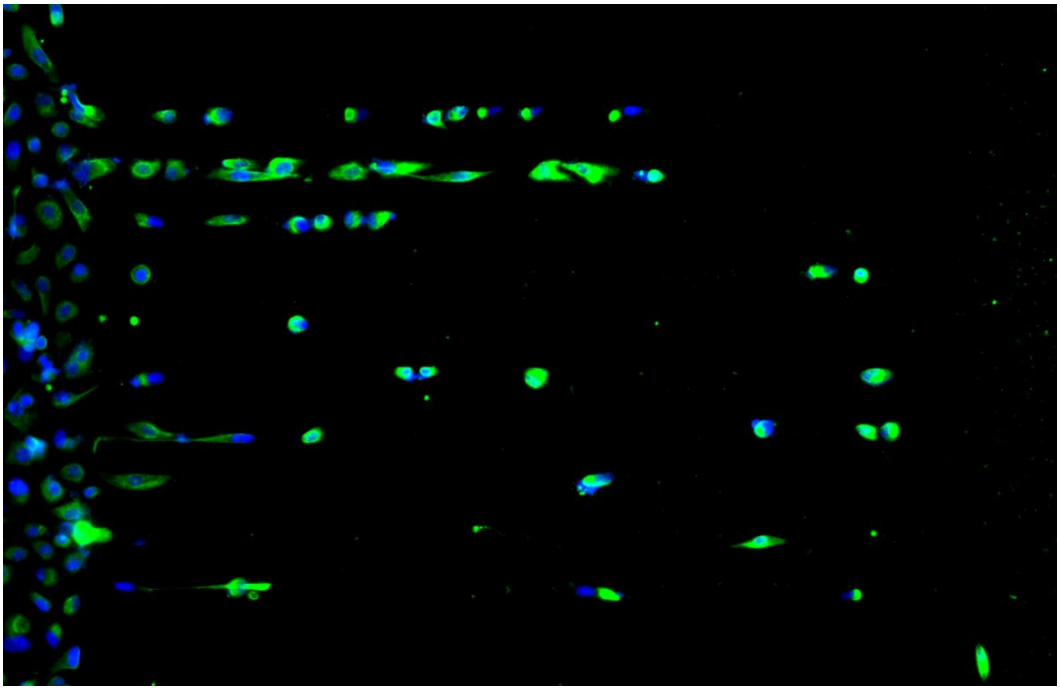

Figure 3-11 PC-3 migration in response to growth medium containing kidney extract

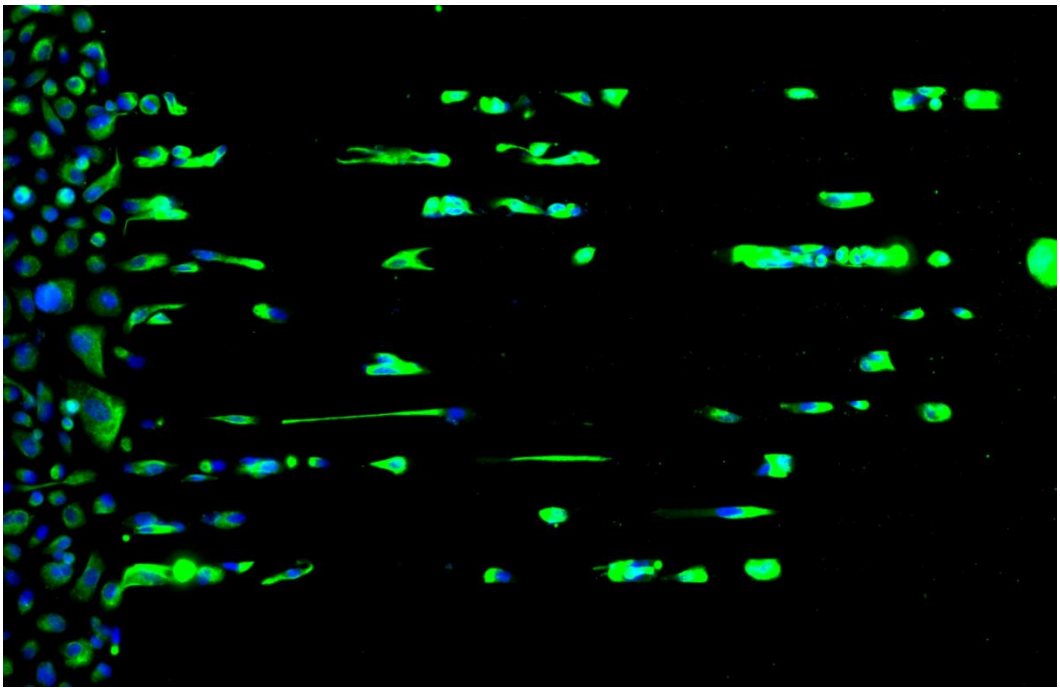

Figure 3-12 PC-3 migration in response to growth medium containing prostate extract

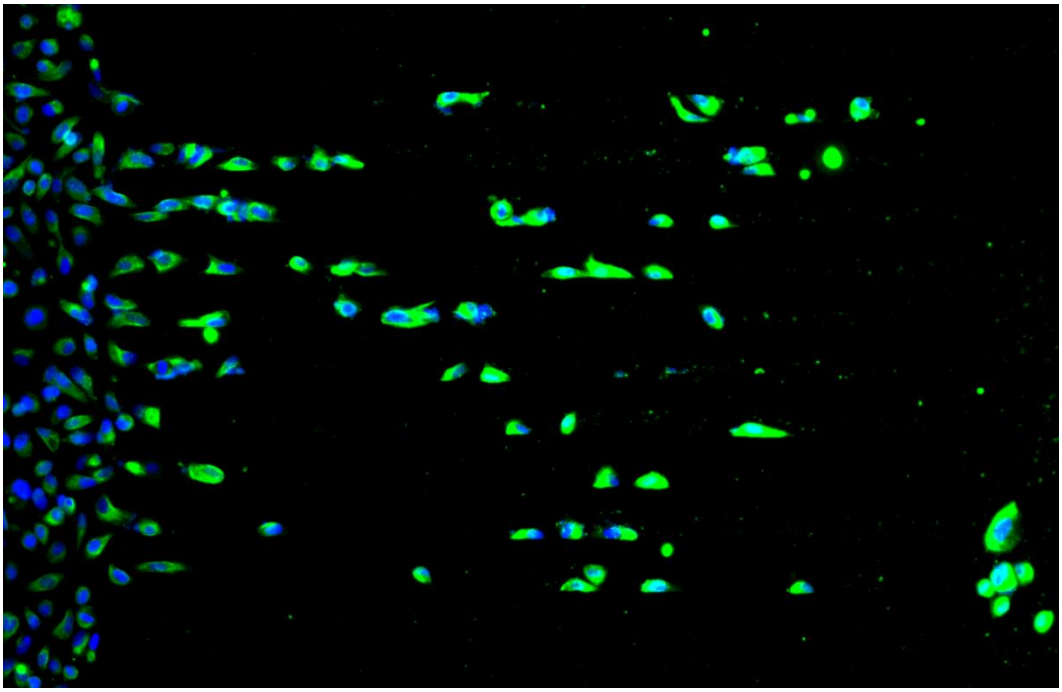

Figure 3-13 PC-3 migration in response to growth medium containing femur extract

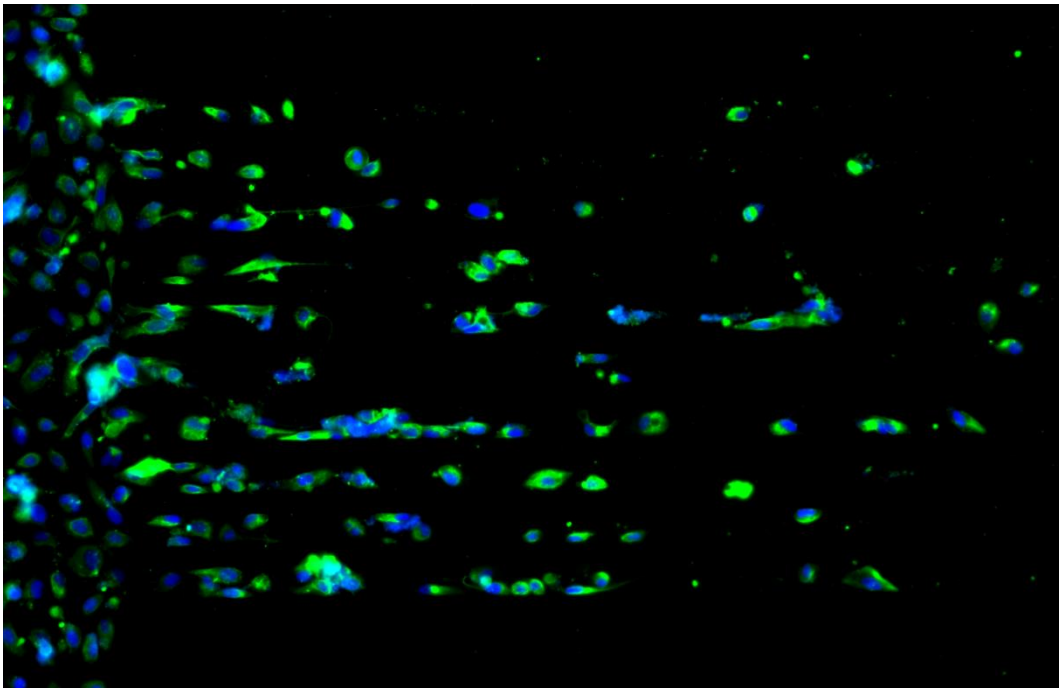

Figure 3-14 PC-3 migration in response to growth medium containing brain extract

Chapter 4

Cellular Migration and Invasion

4.1 Introduction

Migration and invasion enhancer 1(MIEN1) has emerged as a novel promoter of cell migration and invasion. MIEN1 is located in the chromosomal region 17q12-21 which is known to contain several cancer-associated genes, including the ERBB2 or Her-2/*neu* oncogene[74]. MIEN1 is upregulated in a variety of cancers, including breast, prostate, oral, and ovarian cancer, and is associated with poorer prognoses[35-39]. It has been shown that MIEN1 can be prenylated by geranylgeranyltransferase I[75-79]. Prenylated MIEN1 has previously been shown to facilitate actin polymerization and actin-mediated membrane protrusions[76-78, 78-80]. *In vivo*, prenylated MIEN1 has been reported to promote tumor dissemination and metastasis in mouse models[81]. Moreover, MIEN1 can act as a signaling adapter protein to regulate the expression of proteolytic enzymes such as matrix metalloproteinase 9 and urokinase through the Akt/NF-κB pathway[81].

In addition to its prenylation motif, MIEN1 also contains a canonical immunoreceptor tyrosine-based activation motif (ITAM)[81]. ITAM domains have been shown to play an important role in immune cell signal transduction via phosphorylation of the tyrosine residues[78, 81]. However, the function of the ITAM domain in MIEN1 remains unclear.

MIEN1 is thought to promote migration through mediation of epithelial-to-mesenchymal transition, the classical driver of metastasis[76, 82]. However, recent evidence suggests that collective migration, in which cells do not lose their cell-cell adhesion junctions, may also contribute to tumor invasiveness[83-86]. The possibility of MIEN1 facilitating collective migration was also examined.

4.2 MIEN1 Localization in MDA-MB 231

4.2.1 Cell Culture

Human breast carcinoma cell line MDA-MB 231 was cultured in low glucose Dulbecco's Modified Eagle Medium (DMEM) supplemented with 10% FBS, 100 U/ml penicillin, and 100 µg/ml streptomycin. Cells were grown in a standard tissue culture dish. Cells were incubated at 37 °C in 5% CO_2 and 95% standard atmosphere.

4.2.2 Immunocytochemistry

A subconfluent plate of MDA-MB 231 was fixed in a solution of 4% paraformaldehyde in PBS for 20 minutes. The paraformaldehyde was removed and the cells were rinsed twice with PBS for 15 minutes per rinse. The cells were then blocked for 1 hour. Samples were again rinsed twice with PBS. Cells were then incubated with a solution 20 µg/ml of anti-MIEN1 IgG overnight at 4 °C. The primary antibody solution was removed and the sample was again rinsed twice with PBS for 15 minutes per rinse to remove any unbound antibodies. The cells were then incubated in a secondary antibody solution containing 20 µg/ml Alexa 594-labeled goat anti-rabbit immunoglobulin G, and FITC-conjugated phalloidin for 2 hours. The phalloidin served as a stain for filamentous actin. A 5 ng/mL solution of DAPI dissolved in PBS was used as a nuclear stain. Ultraviolet fluorescence microscopy was employed to visualize marker expression and localization within the cells.

4.2.3 Results and Discussion

Immunocytochemical analysis revealed that MIEN1 did not localize to the membrane in MDA-MB 231, nor did it co-localize with actin protrusion sites. The majority of MIEN1 appeared to localize in the cytoplasmic compartment of the cell, as shown in Figure 4-1 below.

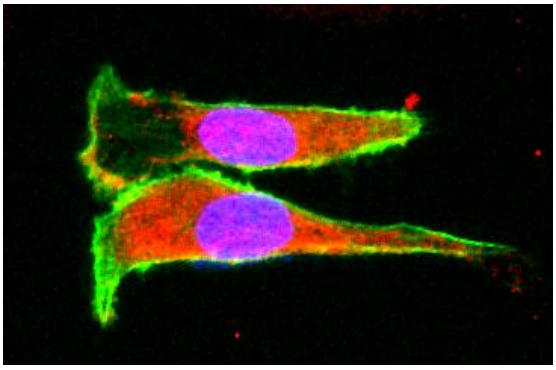

Figure 4-1 Cytosolic MIEN1 (red) localization in MDA-MB 231. F-actin (green) and nucleus (blue) are also shown.

4.3 MIEN1 Knockdown

4.3.1 Cell Culture

Human breast carcinoma cell line MDA-MB 231 was cultured in low glucose Dulbecco's Modified Eagle Medium (DMEM) supplemented with 10% FBS, 100 U/ml penicillin, and 100 µg/ml streptomycin. Cells were grown in a standard 6-well plate to approximately 50% confluence. Cells were incubated at 37 °C in 5% CO_2 and 95% standard atmosphere.

4.3.2 siRNA Transfection

siRNA oligonucleotides with specificity for MIEN1 were obtained from Dharmacon (Lafayette, CO). Sub-confluent MDA-MB 231 cells were serum-starved for 24 hours prior to transfection to enhance cellular uptake of the siRNA. The cells were then transiently transfected with either non-targeting small interfering RNA pool or MIEN1 smart pool siRNA at 100 nM using Lipofectamine RNAiMAX (Life Technologies) in the presence of Reduced Serum Medium (Life Technologies). After 18 hours of incubation with the siRNA, half of the Reduced Serum Medium by volume was replaced by low glucose DMEM supplemented with 10% FBS. Efficient knockdown of MIEN1 requires 72 hours, as shown in Figure 4-2. Thus siRNA-transfected cells were harvested 72 hours

post-transfection for further experiments and validated for protein knockdown by western blotting.

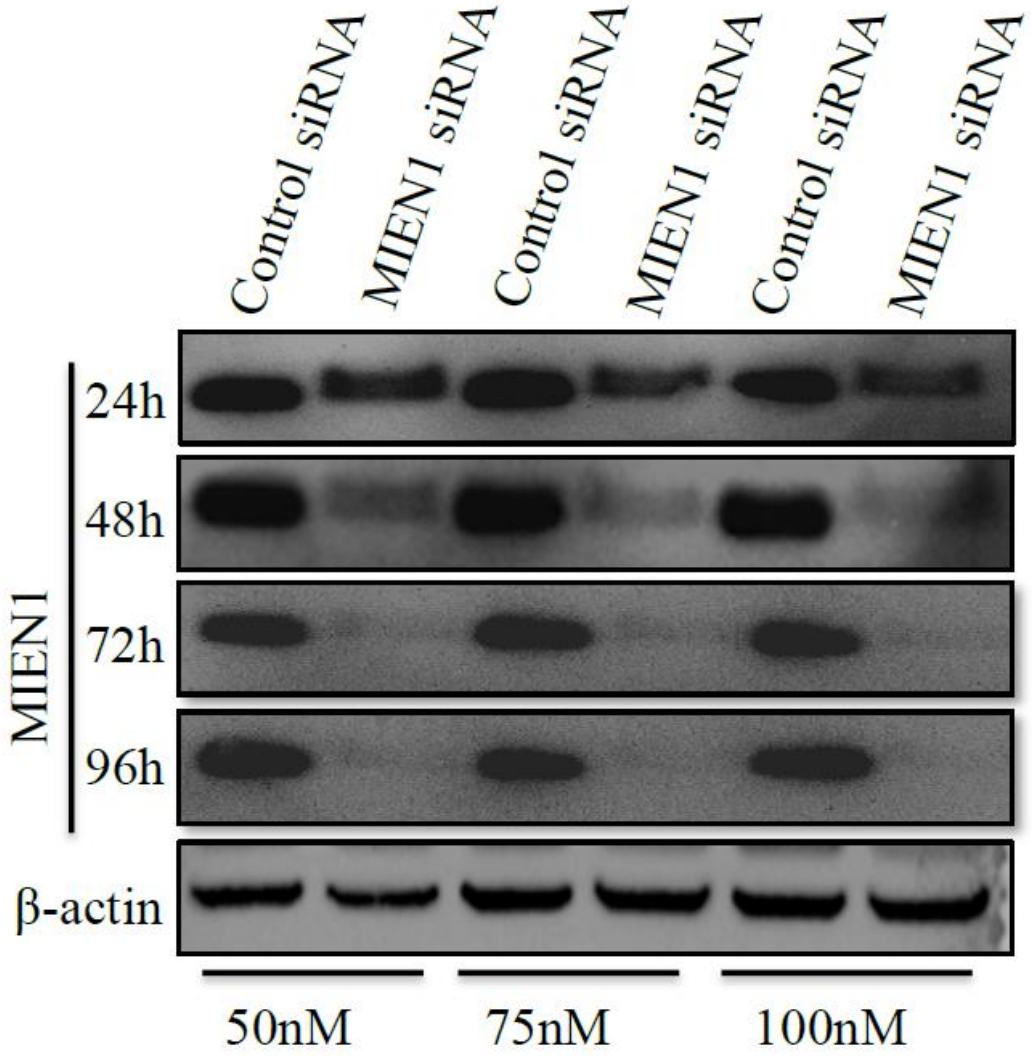

Figure 4-2 Efficient MIEN1 knockdown at 72 hours post-transfection of MDA-MB 231

4.3.3 Cell Seeding

The cell growth medium was aspirated, and the cells were rinsed in sterile phosphate-buffered saline (PBS). The PBS was aspirated and 500 µl 0.25% trypsin EDTA was added to the cells. The cells were stored in the incubator for 5 minutes.

Cellular detachment from the tissue culture substrate was confirmed with the aid of an inverted microscope. The cells were then suspended in 1 ml of FBS-supplemented growth medium to neutralize the trypsin. The cells suspension was transferred to a 15-ml conical vial and was centrifuged at 3500 rpm for 3 minutes. The liquid supernatant was aspirated from the conical vial to leave only the cell pellet. The pellet was resuspended in 1 ml of growth medium. With the aid of a micropipette, 15 µl of the suspension was pipetted into a vial, and 15 µl of 0.4% trypan blue solution was added to the same vial and mixed. A hemocytometer was used to quantify the concentration of the cell suspension.

The stock cell suspension was diluted to create a working cell suspension with a concentration of 1×10^5 cells/ml. The priming growth medium was removed from a cleaned and primed device, and 50 µl of the diluted cell suspension was added to the left well in each well pair to achieve a seeding density of 5×10^3 cells/well. Standard growth medium well was added to the right well in each well pair. For each condition, a total of 8 well pairs were used. The areas of the tissue culture dish that were not covered by the PDMS device were filled with sterile PBS to limit the evaporation of growth medium from the wells. The growth medium was replaced every 48 hours in all wells.

4.3.3 Image Acquisition and Analysis

Brightfield images of the cells within the channels were captured at 100× magnification at 24 hour intervals with a Nikon Ti Eclipse microscope for 96 hours. siRNA-mediated gene knockdown is transient and is effective for only a limited period of time because the siRNA will eventually be enzymatically degraded within the cell. These images were analyzed using AxioVision (Zeiss, USA) to determine the position of the leading cell in each channel relative to the leftmost point of each channel. Channels containing no cells were assigned a value less than 10 µm. The migration distance data

were subsequently organized by day and experimental condition with a MATLAB program, which also converted measurement values lower than 10 μm to 0 μm. The results were written to a Microsoft Excel spreadsheet for further analysis. The number of cells in each channel were counted by hand and entered into a Microsoft Excel spreadsheet.

Results and Discussion

The migration data are presented in Figure 4-3 below.

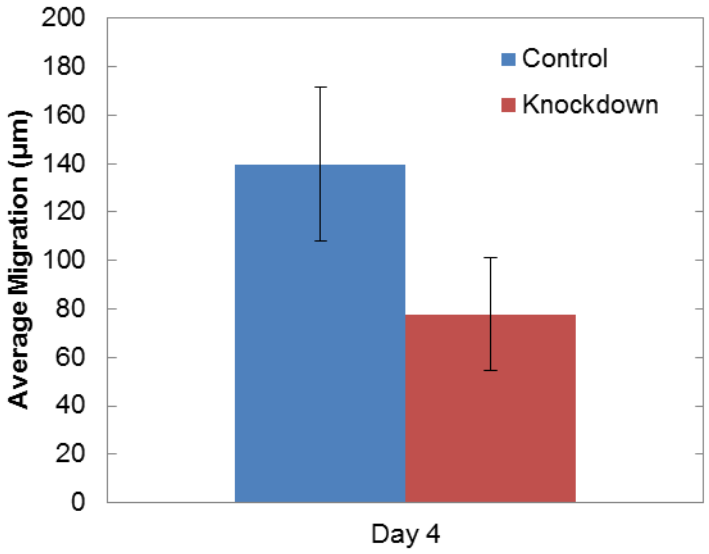

Figure 4-3 Fourth-day migration of MDA-MB 231 transfected with non-targeting or MIEN1-targeting siRNA

Comparison of the average migration distances by a Student's t-test revealed that the difference was not significant (p = 0.057). However, cytotoxicity induced by the transfection reagent may have been a confounding factor in the experiment.

4.4 Influence of MIEN1 Overexpression on Cell Migration

4.4.1 Plasmid Construction

The plasmids used to express MIEN1 proteins were created by sub-cloning PCR-amplified human MIEN1 cDNA into pEGFP-C1 vector as previously described. Site-

directed mutagenesis was performed from the GFP-MIEN1^{WT} template using QuikChange multi-site-directed mutagenesis kit (Stratagene, La jolla, CA). Constructs created were GFP-MIEN1^{WT}, GFP-MIEN1$^{Y39/50F}$ (in which Tyr^{39} and Tyr^{50} are mutated to Phe) and GFP-MIEN1$^{Y39/50F/\Delta 112-115}$ (where amino acids 112-115 in the prenylation domain were deleted in addition to the replacements of Tyr^{39} and Tyr^{50} by Phe). Tyrosine and phenylalanine are structurally similar amino acids. However, tyrosine possesses a hydroxyl group in its side chain that can be phosphorylated whereas phenylalanine does not. All constructs were verified by sequencing. Figure 4-4 displays the resulting amino acid sequences coded by the plasmid constructs.

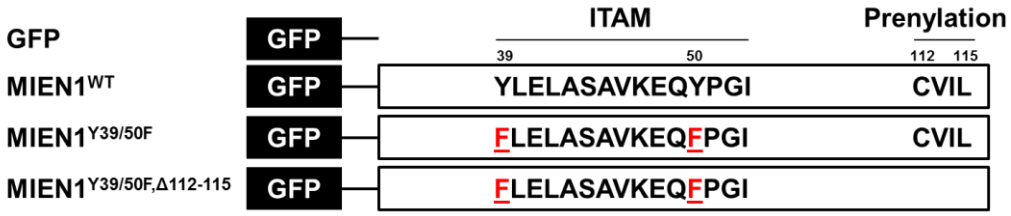

Figure 4-4 Peptide sequence of MIEN1 constructs at ITAM and prenylation domains

4.4.2 Cell Transfection and Culture

MDA-MB 231 cells were transfected with pEGFP-C1 vector or GFP-tagged MIEN1 constructs (GFP-MIEN1^{WT}, GFP-MIEN1$^{Y39/50F}$, GFP-MIEN1$^{Y39/50F,\Delta 112-115}$) using jetPRIME (VWR, Radnor, PA) as recommended by the manufacturer. Stable oligoclonal pools of MDA-MB 231 stably expressing the constructs were generated using G418. G418 is an aminoglycoside antibiotic that inhibits polypeptide synthesis at the elongation step in both prokaryotic and eukaryotic organisms. The plasmid used in the cell transfections also contains a gene that imparts resistance to G418. Thus only cells that were stably transfected can survive for extended periods of exposure to G418. Expression of GFP-tagged MIEN1 constructs were confirmed by western blotting, as shown in Figure 4-5.

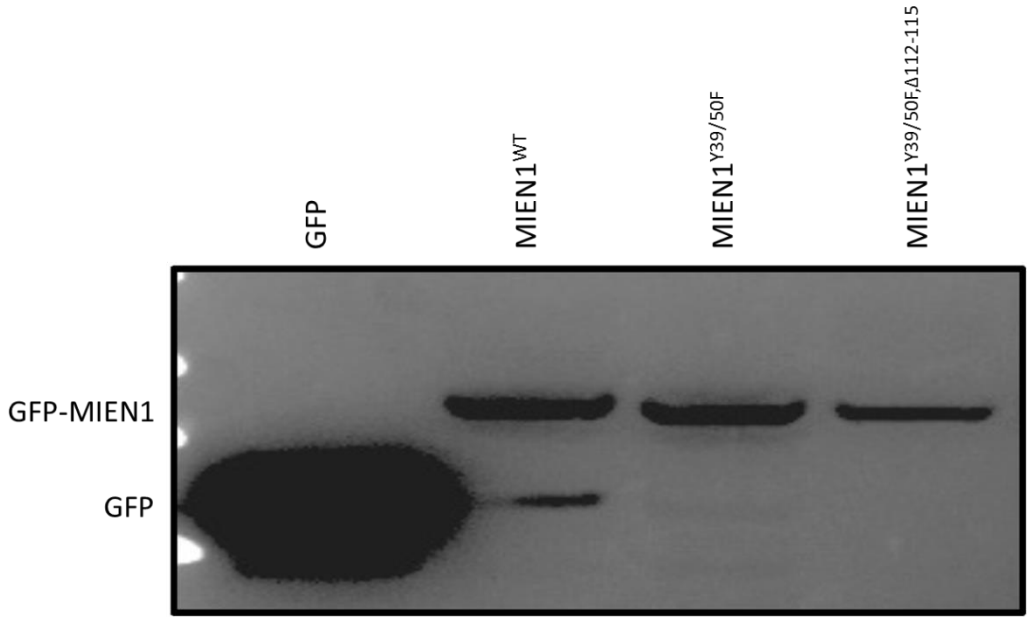

Figure 4-5 Western blot confirming expression of GFP-tagged MIEN1 constructs in MDA-MB 231

Cells were cultured in low glucose Dulbecco's Modified Eagle Medium (DMEM) supplemented with 10% FBS, 100 U/ml penicillin, 100 µg/ml streptomycin, and 600 µg/ml G418. Cells were incubated at 37 °C in 5% CO_2 and 95% standard atmosphere and were grown to 70% confluence.

4.4.3 Cell Seeding

The cell growth medium was aspirated, and the cells were rinsed in sterile phosphate-buffered saline (PBS). The PBS was aspirated, and 500 µl 0.25% trypsin EDTA was added to the cells. The cells were stored in the incubator for 5 minutes. Cellular detachment from the tissue culture substrate was confirmed with the aid of an inverted microscope. The cells were then suspended in 1 ml of FBS-supplemented growth medium to neutralize the trypsin. The cells suspension was transferred to a 15-ml conical vial and was centrifuged at 3500 rpm for 3 minutes. The liquid supernatant was aspirated from the conical vial to leave only the cell pellet. The pellet was resuspended in

1 ml of growth medium. With the aid of a micropipette, 15 µl of the suspension was pipetted into a vial, and 15 µl of 0.4% trypan blue solution was added to the same vial and mixed. A hemocytometer was used to quantify the concentration of the cell suspension.

The stock cell suspension was diluted to create a working cell suspension with a concentration of 1×10^5 cells/ml. The priming growth medium was removed from a cleaned and primed device, and 50 µl of the diluted cell suspension was added to the left well in each well pair to achieve a seeding density of 5×10^3 cells/well. Standard growth medium well was added to the right well in each well pair. For each condition, a total of 16 well pairs were used. The areas of the tissue culture dish that were not covered by the PDMS device were filled with sterile PBS to limit the evaporation of growth medium from the wells. The growth medium was replaced every 48 hours in all wells.

4.4.4 Image Acquisition and Analysis

Brightfield images of the cells within the channels were captured at 100× magnification at 24 hour intervals with a Ti Eclipse Nikon microscope for 120 hours. These images were analyzed using AxioVision (Zeiss, USA) to determine the position of the leading cell in each channel relative to the leftmost point of each channel. Channels containing no cells were assigned a value less than 10 µm. The migration distance data were subsequently organized by day and experimental condition with a MATLAB program, which also converted measurement values lower than 10 µm to 0 µm. The results were written to a Microsoft Excel spreadsheet for further analysis. The number of cells in each channel were counted by hand and entered into a Microsoft Excel spreadsheet. The microscope was equipped with a Bold Line Cage Incubator (Okolab, Italy) and a supply of CO_2. Multipoint time-lapse microscopy was subsequently performed to acquire real-time cell migration data. Images of the microchannels were captured at

100× magnification at 10-minute intervals for a period of 15 hours. The images were then analyzed using ImageJ and CellTracker software to determine the speed and persistence of migrating cells in the channels along a single dimension.

4.4.5 Results and Discussion

At 24 hours from the point of initial cell seeding, very few cells were observed to have entered the channels, and the leading cells had not traveled a great distance. Cell number and migration distance progressively increased until the conclusion of the experiment at 120 hours. At every measured time point, the GFP-MIEN1^{WT}-expressing cells exhibited a significantly greater average distance traveled by the leading cells compared to the GFP-MIEN1$^{Y39/50F}$, GFP-MIEN1$^{Y39/50F/\Delta 112\text{-}115}$-expressing cells ($p < 0.05$). At 72 hours and onward, the GFP-MIEN1^{WT} group had migrated a significantly greater distance across the channels compared to the GFP control vector-expressing cells ($p < 0.05$). A similar profile was observed during cell quantification. Within the GFP-MIEN1^{WT}-expressing group, a greater number of cells were found in the channels at every time point compared to the mutants ($p < 0.05$). At 72 hours, a greater number of GFP-MIEN1^{WT}-expressing cells were found in the channels of the device compared to the GFP control vector-expressing cells ($p < 0.05$). Representative images of each condition at 24, 72, and 120 hours after the initiation of the experiment are presented in Figure 4-6. The cells were colored in manually to enhance visibility. The average distance traveled by the leading cell in each channel and the average number of cells in each channel for each condition is plotted in Figures 4-7 and 4-8, respectively.

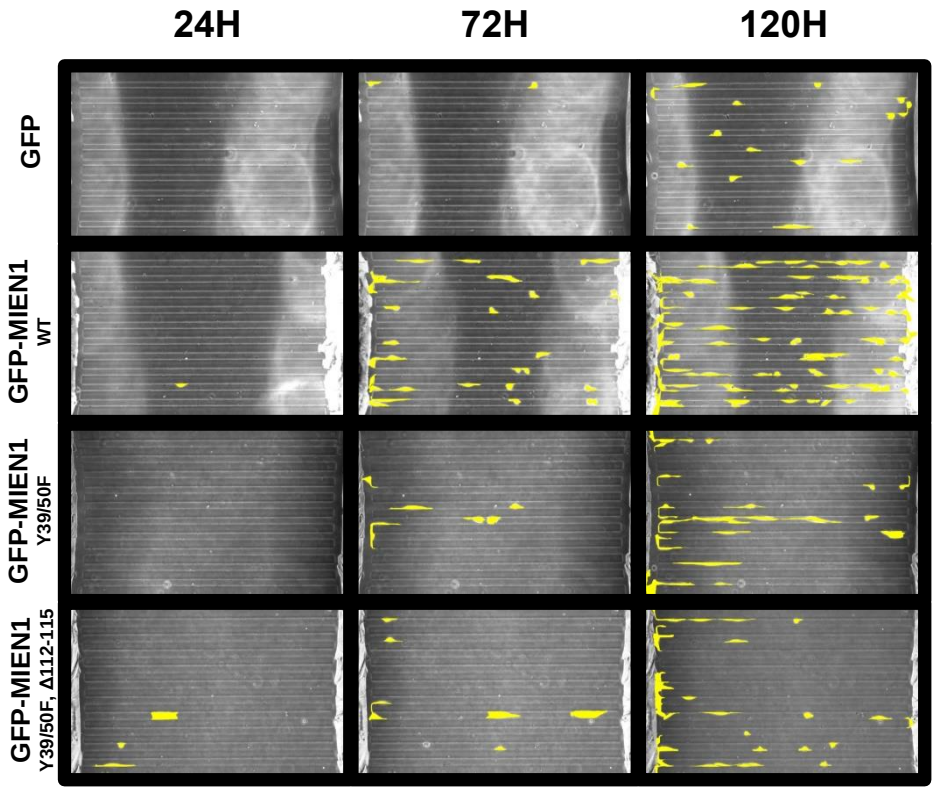

Figure 4-6 Representative images of migration of MDA-MB 231 stably expressing GFP, GFP-MIEN1^{WT}, GFP-MIEN1$^{Y39/50F}$, and GFP-MIEN1$^{Y39/50F, \Delta112-115}$

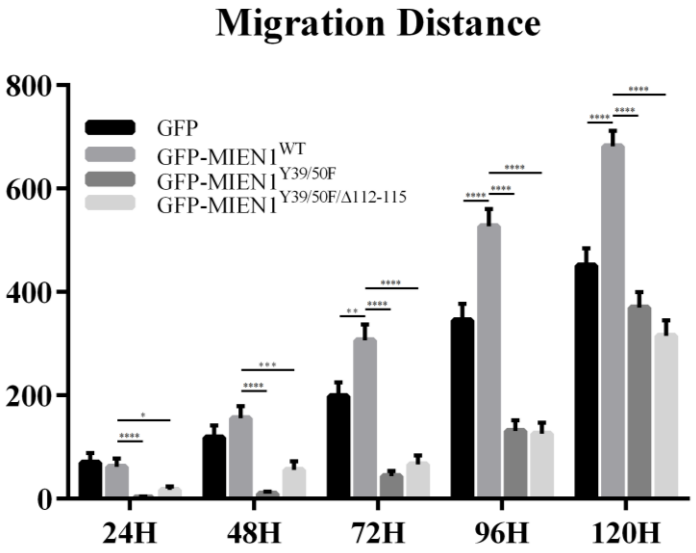

Figure 4-7 Average migration distance of the four strains of MDA-MB 231
*p < 0.05, **p < 0.01, ***p < 0.001, ****p < 0.0001

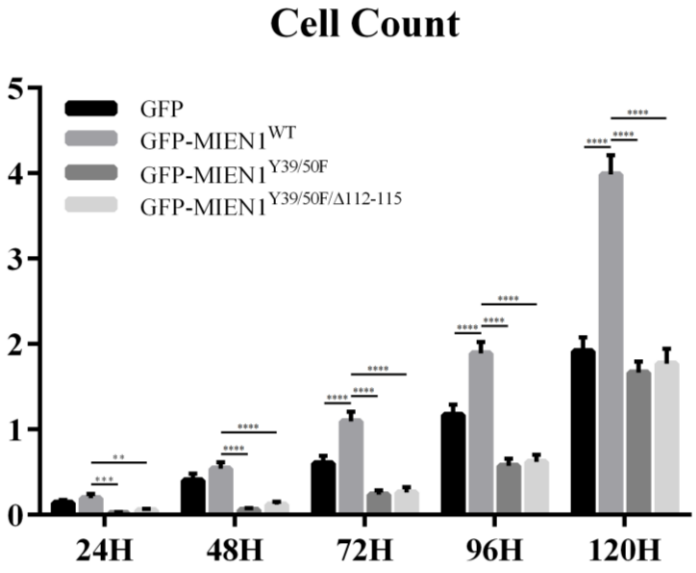

Figure 4-8 Average count of cells in the channels for the four strains of MDA-MB 231
*p < 0.05, **p < 0.01, ***p < 0.001, ****p < 0.0001

Time-lapse microscopy was successfully conducted for 15 hours after the conclusion of the initial 120-hour period. Cell migration speed and persistence were

determined by tracking the movement of cells along the horizontal axis. The formula used to determine cell migration speed is as follows:

$$|\mathrm{v}_n| = |k(p_{n+1} - p_n)|$$

where v_n is the calculated cell velocity at the *n*th time point; *k* signifies a conversion factor of 5.52 μm pixel^{-1} hr^{-1}; and p_n represents the position of the cell along a horizontal axis at the *n*th time point. Persistence was determined by calculating the average distance the cells traveled before reversing direction. The distance traveled prior to direction reversal was calculated using the following equation:

$$d = \sum_{i=a}^{b} |\mathrm{v}_i|$$

where *d* is the distance the cell traveled before changing direction; *a* is the time point at which the cell begins traveling in a given direction; *b* is the time point at which the cell reverses direction; and v_i is cell velocity at the *i*th time interval as calculated by the cell migration speed equation. Using the CellTracker software, individual cells were tracked, and it was observed that cells frequently changed direction over the 15-hour duration. It was found that GFP-MIEN1^{WT}-expressing cells migrated significantly faster and traveled greater distances before changing directions compared to every other group ($p < 0.05$). Interestingly, the increased migration speed does not account for the enhanced directionality of GFP-MIEN1^{WT}-expressing cells. While GFP-MIEN1^{WT}-expressing cells exhibited a 24% higher migration speed compared to the GFP control vector-expressing group, they also displayed a 51% increase in mean migration persistence. Comparisons in speed and persistence between the control group and the mutants revealed no significant difference in either parameter. The migration speed of each group is summarized in Figure 4-9, and the migration persistence of each group is presented in Figure 4-10.

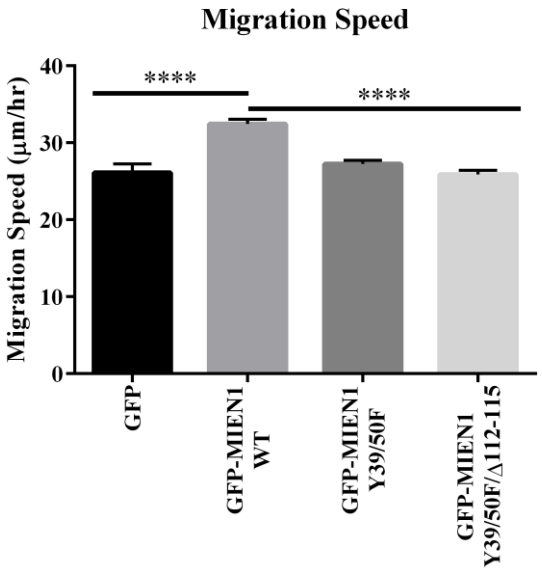

Figure 4-9 Average migration speed of four strains of MDA-MB 231
****$p < 0.0001$

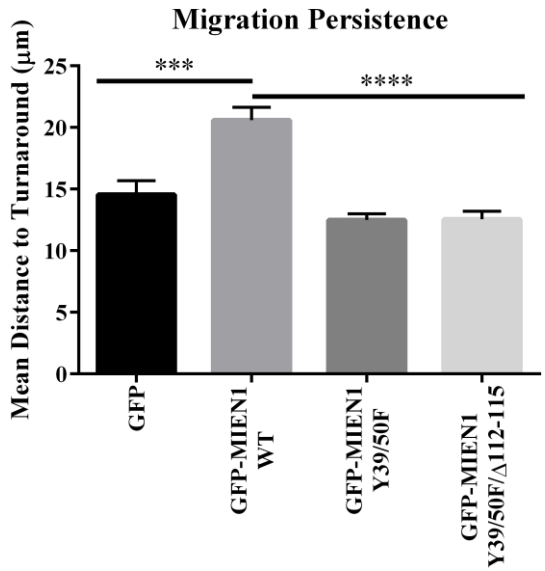

Figure 4-10 Average persistence of four strains of MDA-MB 231
***$p < 0.001$, ****$p < 0.0001$

Given that no chemoattractant was used to draw cells into the channels, these results suggest that increased expression of wild-type MIEN1 enhances the baseline

migratory potential of MDA-MB 231. Since the migration of the prenylation/ITAM double mutant was not significantly different from the ITAM single mutant, these results also indicate that phosphorylation of the ITAM domain is vital to the function of MIEN1.

4.5 MIEN1 and Cell-Cell Adhesion

4.5.1 Cell Culture

Unmodified MDA-MB 231 and MDA-MB 231 stably expressing GFP-MIEN1^{WT}, GFP-MIEN1$^{Y39/50F}$, or GFP-MIEN1$^{Y39/50F/\Delta 112\text{-}115}$ were generated and cultured as described in 4.4.2.

4.5.2 Hanging Drop Assay

MDA-MB 231 transiently transfected with MIEN1-targeting siRNA or nontargeting siRNA were suspended in growth medium at a density of 2.5×10^5 cells/ml. A 20 µl droplet of cell suspensions were placed on the inner surface of the lids of standard 100 mm culture dishes. Sterile PBS was added to the culture dishes to minimize fluid evaporation. The lids were mounted onto their respective dishes to suspend the cell-containing droplets. Cells were imaged with the aid of an inverted microscope 6 hours and 12 hours after lid mounting. Ten random fields were captured, and the average cell cluster size was quantified using ImageJ.

4.5.3 Immunocytochemistry

To further investigate the mechanism by which MIEN1 mediated cell-cell adhesion, immunostaining for e-cadherin, n-cadherin, p120-catenin, and β-catenin was conducted. These proteins play a role in forming adherens junctions between cells. Upon the conclusion of the cell migration assay described in sections 4.4.3 and 4.4.4, the cells were then fixed in a solution of 4% paraformaldehyde in PBS for 20 minutes. The device left mounted on the tissue culture plate to isolate the cells so that multiple antibodies could be used in conjunction. The paraformaldehyde was removed and the cells were

rinsed twice with PBS for 15 minutes per rinse. The cells were then blocked. Samples were again rinsed twice with PBS. Cells were then incubated with a solution containing 20 µg/ml of a primary antibody overnight at 4 °C. The primary antibodies used were anti-e-cadherin, anti-n-cadherin, anti-p120 catenin, and anti-β-catenin. The primary antibody solution was removed and the sample was again rinsed twice with PBS for 15 minutes per rinse to remove any unbound antibodies. The cells were then incubated in a secondary antibody solution of 20 µg/ml rhodamine (TRITC)-labeled goat anti-mouse immunoglobulin G for 2 hours. A 5 ng/mL solution of DAPI dissolved in PBS was used as a nuclear stain. Ultraviolet fluorescence microscopy was employed to visualize marker expression and localization within the cells.

4.5.4 Results and Discussion

Representative images of each condition in the hanging drop assay are shown in Figure 4-11. The results demonstrated that transient siRNA-mediated knockdown of MIEN1 in MDA-MB 231 significantly inhibited the formation of cell clusters in suspension ($p < 0.01$), as shown in 4-12.

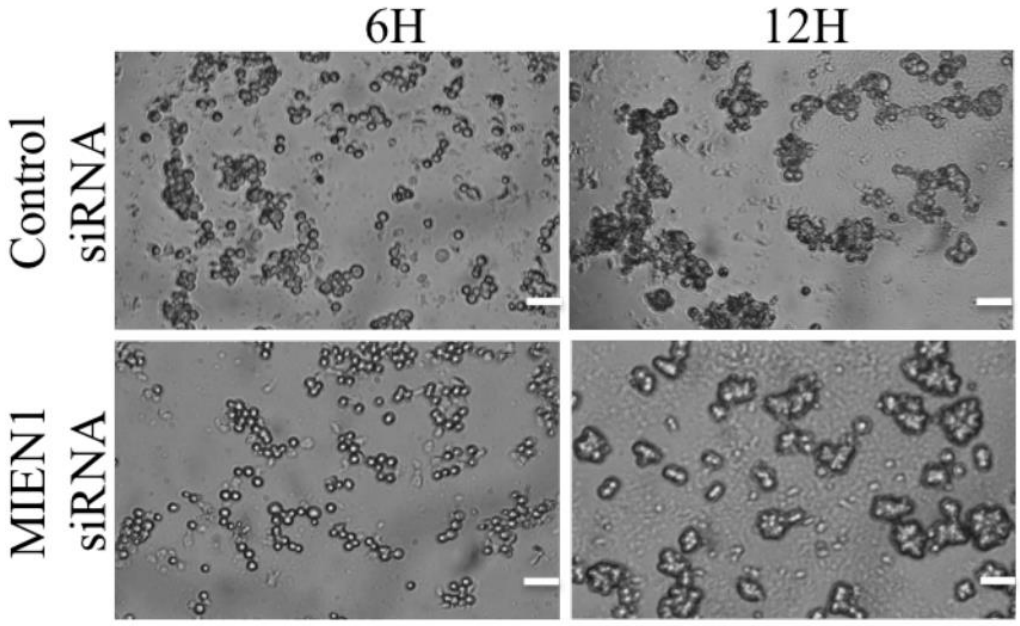

Figure 4-11 Clustering of suspended MDA-MB 231 in the hanging drop assay

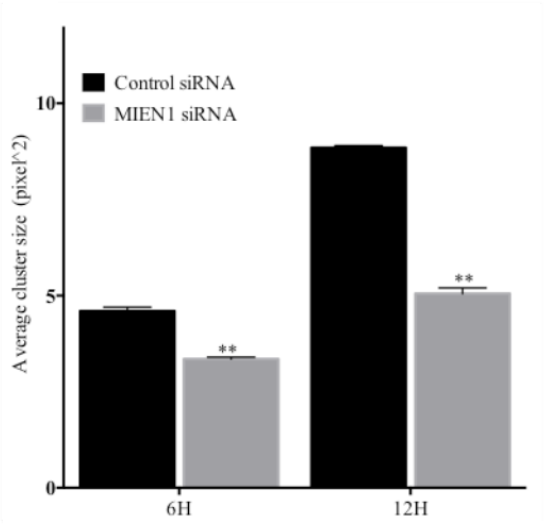

Figure 4-12 Average cluster size of MDA-MB 231 in suspension
*p < 0.05, **p < 0.01

The staining results for e-cadherin, n-cadherin, p120-catenin, and β-catenin are shown in Figures 4-13, 4-14, 4-15, and 4-16, respectively.

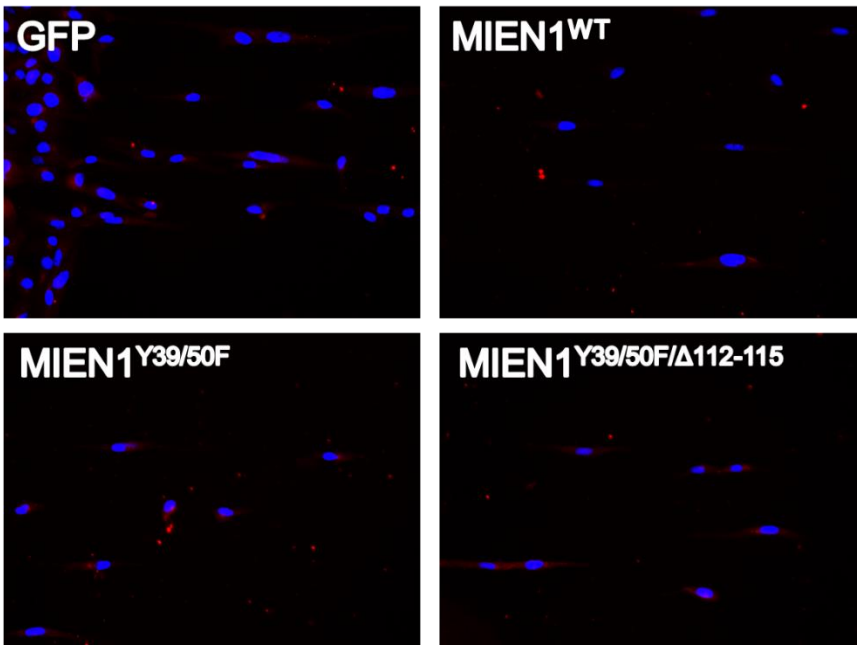

Figure 4-13 Immunofluorescent staining for e-cadherin (red) in four strains of MDA-MB 231 with DAPI (blue) nuclear stain

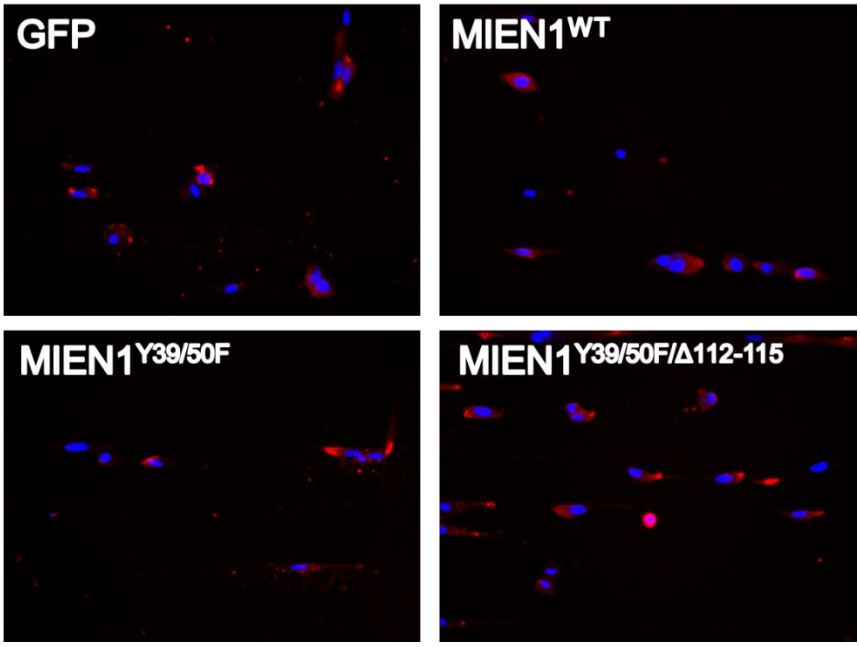

Figure 4-14 Immunofluorescent staining for n-cadherin (red) in four strains of MDA-MB 231 with DAPI (blue) nuclear stain

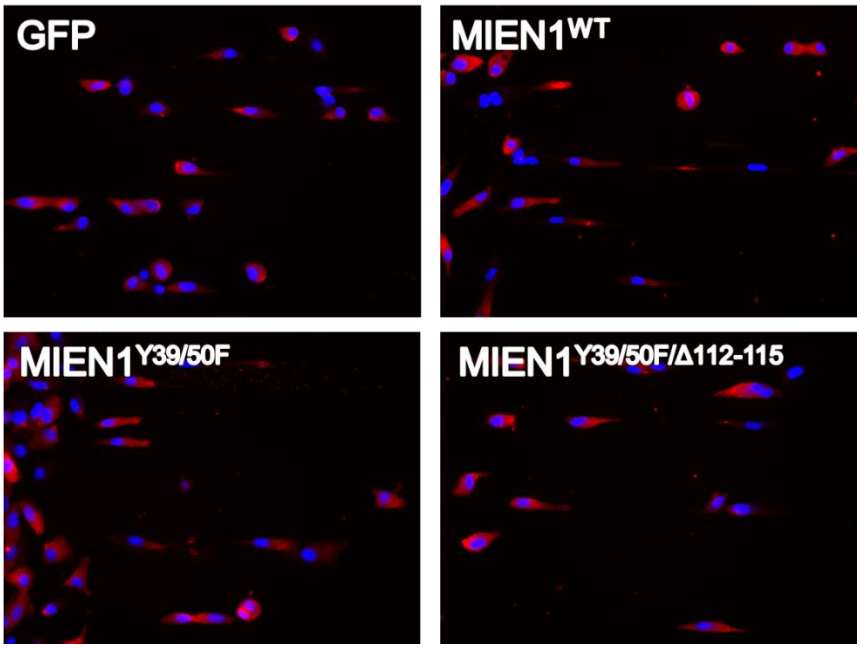

Figure 4-15 Immunofluorescent staining of p120-catenin (red) in four strains of MDA-MB 231 with DAPI (blue) nuclear stain

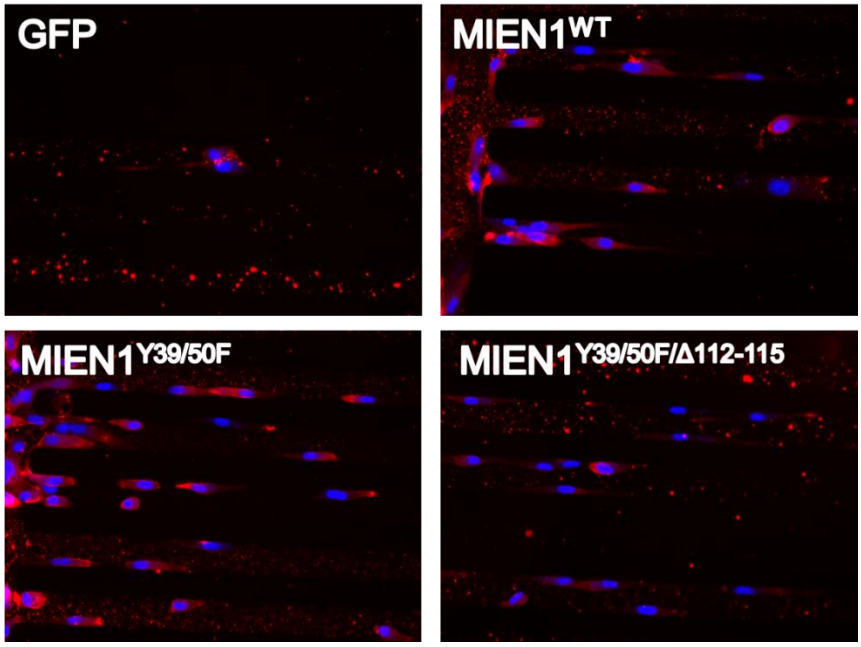

Figure 4-16 Immunofluorescent staining of β-catenin (red) in four strains of MDA-MB 231 with DAPI (blue) nuclear stain

MDA-MB 231 has previously been shown to express very low or no e-cadherin and n-cadherin, which accounts for the weak fluorescent signal of these stains. MIEN1 expression does not appear to alter the expression or localization of either e-cadherin or n-cadherin. P120 catenin and β-catenin are typically membrane-associated proteins. However, ectopic expression has been linked to aberrant cell behavior. Cytoplasmic localization of p120-catenin and β-catenin was observed in all conditions, but there was no discernible difference between the four groups that were examined. Interestingly, some cells in all conditions appeared to display membrane-associated β-catenin, suggesting the possibility of cadherin-mediated cell-cell interactions.

Furthermore, it is known that MIEN1 promotes actin protrusions. Integrins play a significant role in cell-substrate adhesion, and have been shown in some cases to facilitate cell-cell adhesion. The influence of MIEN1 on different cell-cell adhesion mechanisms warrants further investigation. This work demonstrates the possible role that

MIEN1 plays in the progression of cancer and elucidates the importance of a previously unexplored protein domain. These results present a new target for therapies in the ongoing battle to treat invasive and metastatic cancer.

Chapter 5

Conclusions and Future Work

A SU-8 template on a silicon wafer was fabricated using standard photolithography techniques. A PDMS-based microfluidic device was successfully fabricated using standard soft lithography techniques. The device retained its flexibility, surface properties, and optical transparency through multiple cleaning and sterilization cycles, supporting the claim that the system can be reused for multiple experiments without loss of experimental fidelity or repeatability. Additionally, miniaturization allows for multiple samples to be examined on a small device footprint and improves experimental throughput and reduces the amount of potentially expensive reagent required to conduct chemotaxis assays. Finite element analysis modeling of the device in ANSYS 15.0 reveals that stable concentration gradients can be established and maintained across the length of the microchannels without the incorporation of fluid flow. This presents a significant advantage of the discussed microfluidic device over other microfluidic systems that require either fluid flow or frequent growth medium replacement to maintain concentration gradients. It was also shown that many types of gradient profiles can be established using similar devices with different channel configurations. Modeling in ANSYS 15.0 showed that nonlinear gradient profiles can be generated with minor modifications to the original device design. Possible future work includes the fabrication of devices with alternative channel configurations to determine the behavior of cells in response to nonlinear concentration gradients of certain chemicals.

Cellular chemotaxis assays with the microfluidic device were conducted. A linear concentration gradient of EGF from 0 ng/ml to 75 ng/ml across 1000 μm was shown to exert a chemotactic effect on human lung adenocarcinoma A549 and triple negative breast cancer MDA-MB 231. A similar experiment involving the chemotaxis of human

prostate carcinoma PC-3 to 8 μg/ml dilutions of organ lysates in growth medium was also conducted. The results suggest that soluble factors present in certain organs such as the bone and brain exert a strong chemotactic effect on PC-3. This may be of clinical relevance, as prostate cancer has been shown to preferentially metastasize to the bone *in vivo*. Furthermore, immunocytochemistry revealed that vimentin, a mesenchymal biomarker, is upregulated in migrating PC-3 for all conditions. Since epithelial-to-mesenchymal transition is implicated in the adoption of a highly migratory and invasive phenotype in cancer, and since the control also presented similar results, cancer cells may acquire motility through paracrine or autocrine signaling. These results suggest that a small subpopulation of cancer cells may adopt the phenotype necessary to invade neighboring tissues and eventually metastasize. Manual and computational quantification of cell migration was successfully conducted via imaging of the device microchannels.

The role of MIEN1 in promoting cancer cell dissemination was also investigated in a breast cancer model. Immunocytochemistry revealed that MIEN1 does not localize to the membrane in MDA-MB 231 and is instead found in the cytosol. Transient knockdown of MIEN1 by siRNA failed to demonstrate a significant effect in cell migration. However, the cytotoxic effects of the Lipofectamine RNAiMAX transfection reagent may have also inhibited migration. A greater sample size could help establish the effects of MIEN1 knockdown on cell migration. Furthermore, siRNA-mediated knockdown is effective for a limited period of time. An experiment conducted over longer time durations could give more conclusive results, but a more method of gene silencing would be required. Despite this, overexpression of wild-type MIEN1 was shown to significantly increase cell migration. Time lapse microscopy also revealed that GFP-MIEN1^{WT}-expressing cells possessed greater motility and persistence compared to the mutants and control. It was also demonstrated that directed mutation of Tyr at residue 39 and/or 50 to Phe on MIEN1

at the ITAM domain induced the loss of the motility enhancements imparted the wild type of MIEN1. A simultaneous mutation in the ITAM domain and the prenylation domain did not further reduce the motility of the cells compared to alterations to only the ITAM domain. This suggests that phosphorylation of the ITAM domain in MIEN1 by a protein kinase is critical to proper function. Identification of the kinase responsible for phosphorylating MIEN1 would enable further elucidation of the pathways responsible for metastasis. Since MIEN1 expression in normal tissues is low or nonexistent, it could serve as a therapeutic target for the treatment of cancer.

Although the microfluidic platform was used chiefly as a model for cancer metastasis, this system and the techniques discussed in this thesis can be used for a variety of other biological studies. For example, cell migration plays an important role in developmental biology and wound healing. This platform could be used to examine the role of chemical signaling in such phenomena as neurite outgrowth and leukocyte chemotaxis. Moreover, it is conceivable that extracellular matrix gels could be embedded in the wells and/or channels of the device, or that the tissue culture substrate could be modified to generate a surface gradient. This design would permit detailed examinations of complex cell-extracellular matrix interactions and cellular haptotaxis *in vitro*.

Appendix A

Additional Experiments and Procedures

A.1 Scratch Wound Assay

A.1.1 Cell Culture

Human lung adenocarcinoma cell line A549 was cultured in RPMI 1640 supplemented with 10% fetal bovine serum (FBS), 100 U/ml penicillin, and 100 µg/ml streptomycin. Cells were grown in a standard tissue culture dish. Cells were incubated at 37 °C in 5% CO_2 and 95% standard atmosphere.

A.1.2 Cell Seeding

The cell growth medium was aspirated, and the cells were rinsed in sterile phosphate-buffered saline (PBS). The PBS was aspirated, and 500 µl 0.25% trypsin EDTA was added to the cells. The cells were stored in the incubator for 5 minutes. Cellular detachment from the tissue culture substrate was confirmed with the aid of an inverted microscope. The cells were then suspended in 1 ml of FBS-supplemented growth medium to neutralize the trypsin. The cells suspension was transferred to a 15-ml conical vial and was centrifuged at 3500 rpm for 3 minutes. The liquid supernatant was aspirated from the conical vial to leave only the cell pellet. The pellet was resuspended in 1 ml of growth medium. With the aid of a micropipette, 15 µl of the suspension was pipetted into a vial, and 15 µl of 0.4% trypan blue solution was added to the same vial and mixed. A hemocytometer was used to quantify the concentration of the cell suspension.

The volume of cell suspension necessary for 150,000 cells (low density seeding) was dispensed into one well in a six-well plate. The volume of cell suspension necessary for 500,000 cells (high density seeding) was dispensed into a second six-well plate. Both wells were filled with 2 ml standard growth medium. After 24 hours from the initial seeding, the growth medium was replaced with 2 ml of fresh growth medium. Cells were

allowed to grow for an additional 48 hours to allow for the formation of a confluent monolayer in both wells.

The growth medium was then aspirated from the wells, and voids were formed in the confluent monolayer with the aid of a micropipette tip. The cells were rinsed twice in 1 ml of standard growth medium to remove any dislodged cells, and 2 ml of fresh growth medium was added to the wells.

A.1.3 Image Acquisition and Analysis

Cells were transferred to a Nikon Ti Eclipse inverted microscope. The microscope was equipped with a Bold Line Cage Incubator (Okolab, Italy) and a supply of CO_2. Multipoint time-lapse microscopy was subsequently performed to acquire real-time cell migration data. Four scratch zones in each condition were captured at 100× magnification at 10-minute intervals for a period of 16 hours. This was performed to ensure that the position of the field of view did not shift between images.

The images were converted from the native ND2 format into a series of TIFF files using ImageJ. The images were rotated to orient the boundaries scratch in either a vertical or horizontal position and were then cropped to a size of 850×850 pixels. Image rotation and cropping were performed to ensure the consistency of the length of the wound region between different images. For example, a diagonally-oriented wound in a rectangular field of view would have a longer wound edge compared to a horizontally or vertically-oriented wound, and thus closure of the wound by the same amount would result in a higher apparent value for the diagonally-oriented wound. Edge detection and particle analysis was performed in ImageJ to determine the fractional area of the void in the cell monolayer. This analysis was performed at the start and end point images. The difference in the wound area between the two time points was used to determine the extent of wound closure. Figures A-1 and A-2 are an example of the process.

A.1.4 Results and Dicussion

With 4 image samples from each condition, the wound area closure was quantified. A Student's t-test was performed to calculate the difference in wound closure between the two seeding conditions, and it was found that the wounds in the high density seeding condition closed more rapidly than the wounds in the low density seeding condition ($p < 0.01$). The results are summarized in Figure A-3.

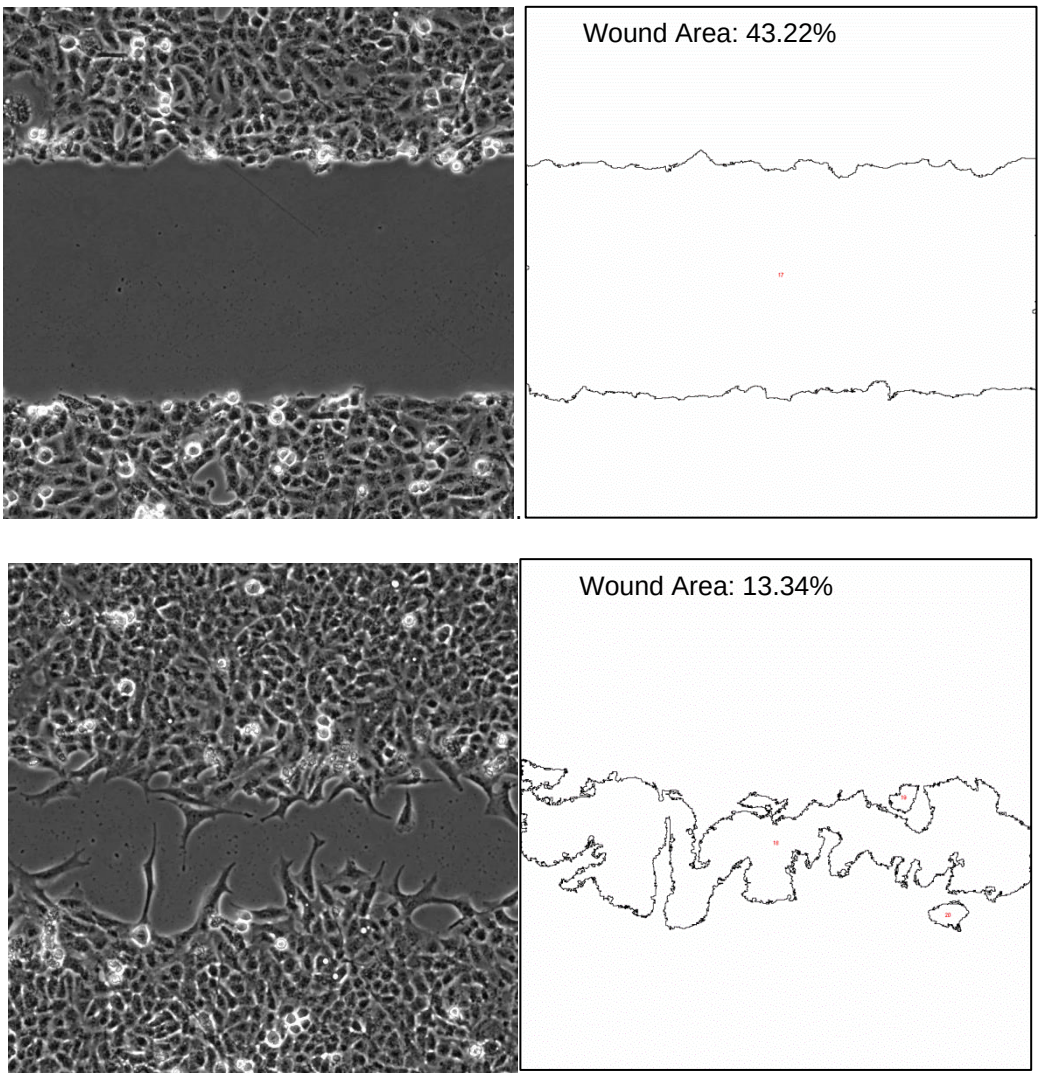

Figure A-1 A549 wound closure with initial seeding of 150,000 cells

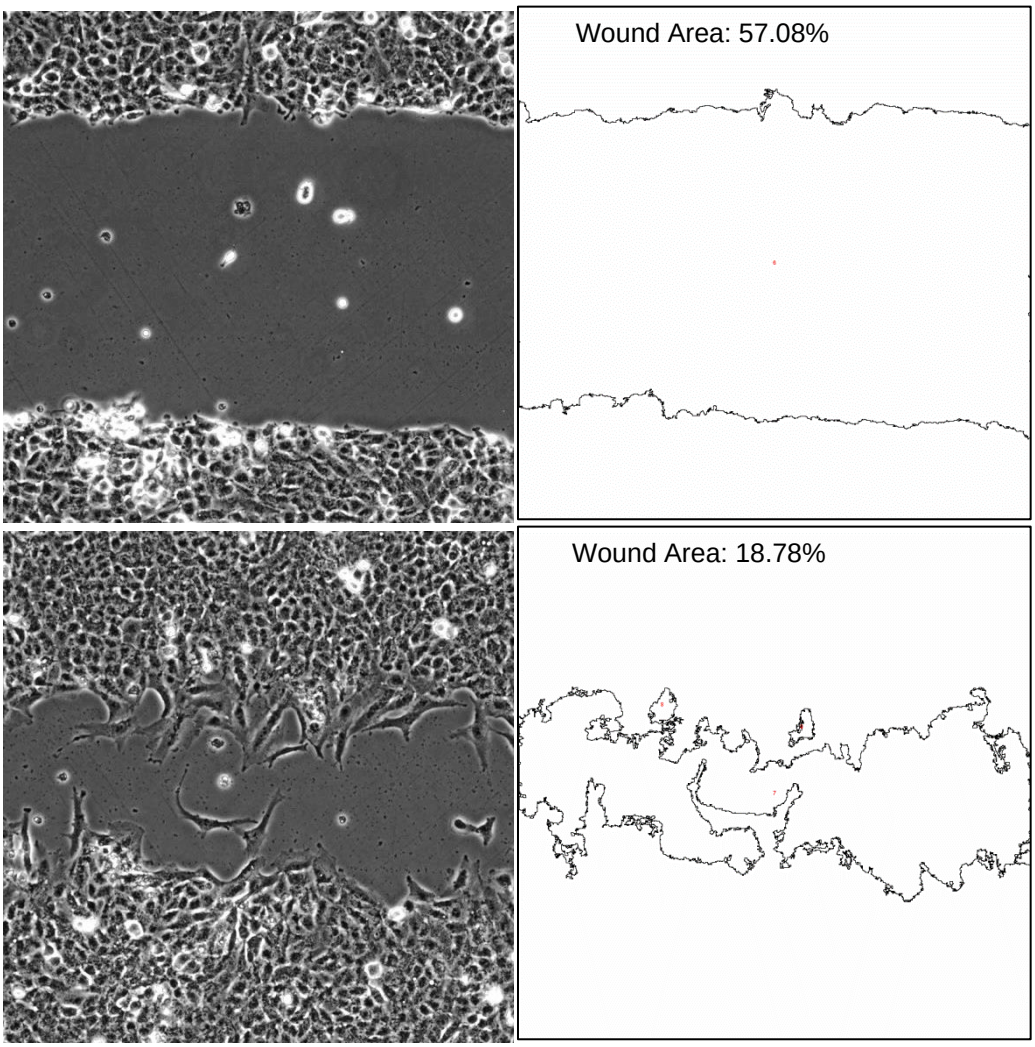

Figure A-2 A549 wound closure with initial seeding of 500,000 cells

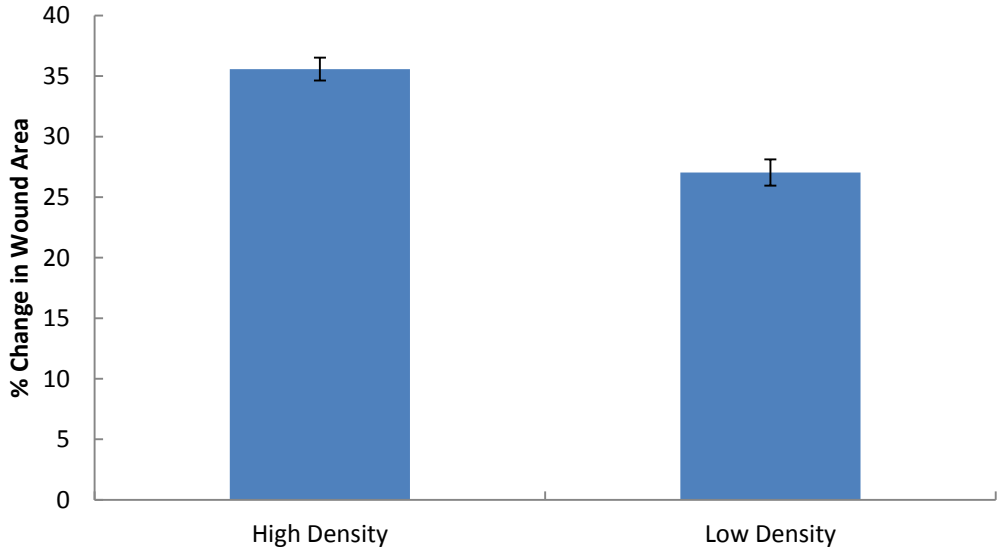

Figure A-3 Change in wound area as a percentage of the total image field

This can be problematic because both wells were considered to have developed a confluent monolayer at the same time point. A difference in judgment of what constitutes a fully confluent culture could differ from person to person, and thus introduces a potential source of subjective bias into the experiment. Additionally, the pipette tips used to create the scratches in Figures A-1 and A-2 were the same size and created by the same manufacturer. However, there is an obvious difference in the width of the scratch regions. Thus it may be difficult to compare results from two scratch wound assays.

Appendix B

Miscellaneous Code

The following text is an AHK script written for AutoHotKey to automate several repetitive tasks during cell migration image processing. This code is compatible with AxioVision 4.9.1 and has been successfully tested on multiple computers with various monitor resolutions.

```
#IfWinActive, AxioVision
{
   a::
   IfWinActive, AxioVision
   {
      MouseMove,300,120,0
      Click
      WinWaitActive,Scalings
      MouseMove,150,100,0
   }
   return
   s::
   IfWinActive, AxioVision
   {
      MouseGetPos,X,Y
      MouseMove,410,120,0
      Click
      MouseMove,%X%,%Y%,0
   }
   return
   d::
   IfWinActive, AxioVision
   {
      MouseMove,385,45,0
      Click
      MouseMove,445,215,0
      Click
      WinWaitActive, Create Data Table
      MouseMove,100,645,0
      Click
      WinWaitActive, Save
      Send DEV
   }
   return
   f::
   IfWinActive, AxioVision
   {
      MouseGetPos,X,Y
      MouseMove,410,120,0
      Click
      MouseMove,%X%,%Y%,0
      Click
      MouseMove,-5,0,0,R
      Click
      MouseMOve,0,-5,0,R
      Click
   }
   return
   g::
   IfWinActive, AxioVision
   {
        MouseGetPos,X,Y
        MouseMove,1594,153,0
        Click
        MouseMove,%X%,%Y%,0
   }
   return
}
```

The corresponding shortcut keys for the AHK script above are displayed in the following table. It should be noted that the SteREO toolbar must be visible in its default position for these shortcut keys to function properly. It should also be noted that using the shortcut keys to create a data table will temporarily disable the use of other shortcut keys until the save window has been opened.

Table B-1 List of shortcut keys and functions

a	Opens the Scalings Control window
s	Selects the Length button
d	Creates a data table
f	Creates a dummy measurement at the cursor position
g	Closes the current image or data table file

The following MATLAB code was used to retrieve and process the CSV files generated by the AxioVision software.

```
userPath = input('Enter complete path of the folder containing .csv files: ','s');
%prompt for folder directory
cd(userPath); %change current path to user-inputted folder directory

numDays = input('\nDuration of experiment (days): '); %prompt for variables to use later
numDevs = input('\nNumber of devices used: ');
numCond = input('\nNumber of experimental conditions: ');

fileList = getAllFiles(userPath); %get the file list
numFiles = numDays * numDevs;
numGroups = numDays * numCond;
usedFiles = cell(numFiles,1);

groups = cell(numCond,1); %for group management
groupDay = cell(numGroups,1); %for group management at a day-to-day level
groupAvg = cell(numGroups,1); %for numerical analysis
groupDev = cell(numGroups,1); %for numerical analysis
avgPlotter = zeros(numCond, numDays);
devPlotter = zeros(numCond, numDays);
groupCounter = 0;
anotherCounter = 0;
fileCount = 0;

for g = 1:numCond
    for h = 1:numDays
        groupCounter = groupCounter + 1;
        groupDay{groupCounter} = strcat('day',int2str(h),'grp',int2str(g));
        eval([groupDay{groupCounter} '= [];']);
    end
end

for i = 1:numDays %first level: day #
    for j = 1:numDevs %second level: device #
        for k = 1:length(fileList) %for loop to search to see if device j exists
            if((~isempty(strfind(lower(fileList{k}),strcat('day',int2str(i),'\')))))
%make sure you're in the right folder
```

```
if((~isempty(strfind(lower(fileList{k}),strcat('dev',int2str(j),'.csv'))))) %find the
file
                    v = genvarname({strcat('day',num2str(i),'dev',int2str(j),'_')});
%create a variable named day#dev#;
                    eval([v{1} '= xlsread(fileList{k},''E3:E12'');']); %read the
measurements into day#dev#
                    fileCount = fileCount + 1;
                    usedFiles{fileCount} = v{1}; %generate a list of all the variable
names used
                    for l = 1:length(eval([v{1}])) %make small measurements zero
                        if(eval([v{1} '(l) < 10']))
                            eval([v{1} '(l) = 0;']);
                        end
                        if(eval([v{1} '(l) > 1000'])) %cap large measurements at 1000
                            eval([v{1} '(l) = 1000;']);
                        end
                    end
                end
            end
        end
    end
end
disp('Don''t touch anything on your keyboard! This part takes time, and the program is
working as expected (probably).\n')

for m = 1:numCond
    userGroup = input(strcat('Enter device numbers for Group ',int2str(m),' in [a b c d
... ] format: ')); %user prompt for the device numbers
    groups{m} = strcat('group',int2str(m)); %what does this line do?
    for n = 1:numDays %search for the correct day
        anotherCounter = anotherCounter + 1;
        for o = 1:numFiles
            for p = 1:length(userGroup) %search for the correct device numbers

if(~isempty(strfind(usedFiles{o},strcat('day',int2str(n),'dev',int2str(userGroup(p)),'_'
)))) %if a correct device is found...
                    eval([groupDay{anotherCounter} '=
cat(1,eval([groupDay{anotherCounter}]),eval([usedFiles{o}]));']);
                end
            end
        end
    end
end

for q = 1:numGroups %create an array of variable names to store averages and standard
deviations
    groupAvg{q} = strcat(groupDay{q},'avg');
    groupDev{q} = strcat(groupDay{q},'dev');
    eval([groupAvg{q} '= mean(eval([groupDay{q}]));'])
    eval([groupDev{q} '= std(eval([groupDay{q}]));'])
end

for r = 1:numCond %assign appropriate averages and standard deviations to given groups
    for s = 1:numDays
        for t = 1:numGroups

if(~isempty(strfind(groupAvg{t},strcat('day',int2str(s),'grp',int2str(r),'avg'))))
                avgPlotter(r,s) = eval([groupAvg{t}]);
            end

if(~isempty(strfind(groupDev{t},strcat('day',int2str(s),'grp',int2str(r),'dev'))))
                devPlotter(r,s) = eval([groupDev{t}]);
            end
        end
    end
```

```
end
errPlotter = devPlotter./sqrt(numDevs/numCond); %assumes that the sample size for each
condition is the same
barweb(avgPlotter,errPlotter); %plot the results
```

The MATLAB code above requires two additional functions: getAllFiles and barweb. These functions were acquired from the file exchange on the MathWorks website. The MATLAB code for the getAllFiles function is reproduced below.

```
function fileList = getAllFiles(dirName)

  dirData = dir(dirName);      %# Get the data for the current directory
  dirIndex = [dirData.isdir];  %# Find the index for directories
  fileList = {dirData(~dirIndex).name}';  %'# Get a list of the files
  if ~isempty(fileList)
    fileList = cellfun(@(x) fullfile(dirName,x),...  %# Prepend path to files
                       fileList,'UniformOutput',false);
  end
  subDirs = {dirData(dirIndex).name};  %# Get a list of the subdirectories
  validIndex = ~ismember(subDirs,{'.','..'});  %# Find index of subdirectories
                                               %#   that are not '.' or '..'
  for iDir = find(validIndex)                  %# Loop over valid subdirectories
    nextDir = fullfile(dirName,subDirs{iDir});    %# Get the subdirectory path
    fileList = [fileList; getAllFiles(nextDir)];  %# Recursively call getAllFiles
  end

end
```

The MATLAB code for the barweb function used to generate a preliminary bar graph is presented below.

```
function handles = barweb(barvalues, errors, width, groupnames, bw_title, bw_xlabel,
bw_ylabel, bw_colormap, gridstatus, bw_legend, error_sides, legend_type)

if nargin < 2
    error('Must have at least the first two arguments:  barweb(barvalues, errors, width,
groupnames, bw_title, bw_xlabel, bw_ylabel, bw_colormap, gridstatus, bw_legend,
barwebtype)');
elseif nargin == 2
    width = 1;
    groupnames = 1:size(barvalues,1);
    bw_title = [];
    bw_xlabel = [];
    bw_ylabel = [];
    bw_colormap = jet;
    gridstatus = 'none';
    bw_legend = [];
    error_sides = 2;
    legend_type = 'plot';
elseif nargin == 3
    groupnames = 1:size(barvalues,1);
    bw_title = [];
    bw_xlabel = [];
    bw_ylabel = [];
    bw_colormap = jet;
    gridstatus = 'none';
    bw_legend = [];
    error_sides = 2;
    legend_type = 'plot';
elseif nargin == 4
```

```
    bw_title = [];
    bw_xlabel = [];
    bw_ylabel = [];
    bw_colormap = jet;
    gridstatus = 'none';
    bw_legend = [];
    error_sides = 2;
    legend_type = 'plot';
elseif nargin == 5
    bw_xlabel = [];
    bw_ylabel = [];
    bw_colormap = jet;
    gridstatus = 'none';
    bw_legend = [];
    error_sides = 2;
    legend_type = 'plot';
elseif nargin == 6
    bw_ylabel = [];
    bw_colormap = jet;
    gridstatus = 'none';
    bw_legend = [];
    error_sides = 2;
    legend_type = 'plot';
elseif nargin == 7
    bw_colormap = jet;
    gridstatus = 'none';
    bw_legend = [];
    error_sides = 2;
    legend_type = 'plot';
elseif nargin == 8
    gridstatus = 'none';
    bw_legend = [];
    error_sides = 2;
    legend_type = 'plot';
elseif nargin == 9
    bw_legend = [];
    error_sides = 2;
    legend_type = 'plot';
elseif nargin == 10
    error_sides = 2;
    legend_type = 'plot';
elseif nargin == 11
    legend_type = 'plot';
end

change_axis = 0;
ymax = 0;

if size(barvalues,1) ~= size(errors,1) || size(barvalues,2) ~= size(errors,2)
    error('barvalues and errors matrix must be of same dimension');
else
    if size(barvalues,2) == 1
        barvalues = barvalues';
        errors = errors';
    end
    if size(barvalues,1) == 1
        barvalues = [barvalues; zeros(1,length(barvalues))];
        errors = [errors; zeros(1,size(barvalues,2))];
        change_axis = 1;
    end
    numgroups = size(barvalues, 1); % number of groups
    numbars = size(barvalues, 2); % number of bars in a group
    if isempty(width)
        width = 1;
    end
```

```
    % Plot bars
    handles.bars = bar(barvalues, width,'edgecolor','k', 'linewidth', 2);
    hold on
    if ~isempty(bw_colormap)
        colormap(bw_colormap);
    else
        colormap(jet);
    end
    if ~isempty(bw_legend) && ~strcmp(legend_type, 'axis')
        handles.legend = legend(bw_legend, 'location', 'best', 'fontsize',12);
        legend boxoff;
    else
        handles.legend = [];
    end

    % Plot errors
    for i = 1:numbars
        x =get(get(handles.bars(i),'children'), 'xdata');
        x = mean(x([1 3],:));
        handles.errors(i) = errorbar(x, barvalues(:,i), errors(:,i), 'k', 'linestyle',
'none', 'linewidth', 2);
        ymax = max([ymax; barvalues(:,i)+errors(:,i)]);
    end

    if error_sides == 1
        set(gca,'children', flipud(get(gca,'children')));
    end

    ylim([0 ymax*1.1]);
    xlim([0.5 numgroups-change_axis+0.5]);

    if strcmp(legend_type, 'axis')
        for i = 1:numbars
            xdata = get(handles.errors(i),'xdata');
            for j = 1:length(xdata)
                text(xdata(j),  -0.03*ymax*1.1, bw_legend(i), 'Rotation', 60,
'fontsize', 12, 'HorizontalAlignment', 'right');
            end
        end
        set(gca,'xaxislocation','top');
    end

    if ~isempty(bw_title)
        title(bw_title, 'fontsize',14);
    end
    if ~isempty(bw_xlabel)
        xlabel(bw_xlabel, 'fontsize',14);
    end
    if ~isempty(bw_ylabel)
        ylabel(bw_ylabel, 'fontsize',14);
    end

    set(gca, 'xticklabel', groupnames, 'box', 'off', 'ticklength', [0 0], 'fontsize',
12, 'xtick',1:numgroups, 'linewidth', 2,'xgrid','off','ygrid','off');
    if ~isempty(gridstatus) && any(gridstatus == 'x')
        set(gca,'xgrid','on');
    end
    if ~isempty(gridstatus) && any(gridstatus ==  'y')
        set(gca,'ygrid','on');
    end

    handles.ax = gca;

    hold off
end
```

References

[1] V. V. Abhyankar, M. W. Toepke, C. L. Cortesio, M. A. Lokuta, A. Huttenlocher and D. J. Beebe. A platform for assessing chemotactic migration within a spatiotemporally defined 3D microenvironment *Lab. Chip 8(9),* pp. 1507-1515. 2008.

[2] C. J. Campbell and B. A. Grzybowski. Microfluidic mixers: From microfabricated to self-assembling devices *Philos. Trans. A. Math. Phys. Eng. Sci. 362(1818),* pp. 1069-1086. 2004.

[3] J. Cha, J. Kim, S. Ryu, J. Park, Y. Jeong, S. Park, S. Park, H. C. Kim and K. Chun. A highly efficient 3D micromixer using soft PDMS bonding *J Micromech Microengineering 16(9),* pp. 1778-1782. 2006.

[4] J. Diao, L. Young, S. Kim, E. A. Fogarty, S. M. Heilman, P. Zhou, M. L. Shuler, M. Wu and M. P. DeLisa. A three-channel microfluidic device for generating static linear gradients and its application to the quantitative analysis of bacterial chemotaxis *Lab. Chip 6(3),* pp. 381-388. 2006.

[5] D. C. Duffy, J. C. McDonald, O. J. A. Schueller and G. M. Whitesides. Rapid prototyping of microfluidic systems in poly(dimethylsiloxane) *Anal. Chem. 70(23),* pp. 4974-4984. 1998.

[6] M. Ghitun, E. Bonneil, M. Fortier, H. Yin, K. Killeen and P. Thibault. Integrated microfluidic devices with enhanced separation performance: Application to phosphoproteome analyses of differentiated cell model systems *Journal of Separation Science 29(11),* pp. 1539-1549. 2006.

[7] J. Harris, H. Lee, B. Vahidi, C. Tu, D. Cribbs, C. Cotman and N. L. Jeon. Non-plasma bonding of PDMS for inexpensive fabrication of microfluidic devices *J. Vis. Exp. (9):410. doi(9),* pp. 410. 2007.

[8] D. E. Ingber. Cellular mechanotransduction: Putting all the pieces together again *The FASEB Journal 20(7),* pp. 811-827. 2006.

[9] D. Irimia and M. Toner. Spontaneous migration of cancer cells under conditions of mechanical confinement *Integr. Biol. (Camb) 1(8-9),* pp. 506-512. 2009.

[10] D. Irimia, D. A. Geba and M. Toner. Universal microfluidic gradient generator *Anal. Chem. 78(10),* pp. 3472-3477. 2006.

[11] N. L. Jeon, S. K. W. Dertinger, D. T. Chiu, I. S. Choi, A. D. Stroock and G. M. Whitesides. Generation of solution and surface gradients using microfluidic systems *Langmuir 16(22),* pp. 8311-8316. 2000.

[12] N. Li Jeon, H. Baskaran, S. K. Dertinger, G. M. Whitesides, L. Van de Water and M. Toner. Neutrophil chemotaxis in linear and complex gradients of interleukin-8 formed in a microfabricated device *Nat. Biotechnol. 20(8),* pp. 826-830. 2002.

[13] J. Li. Application of microfluidic devices to proteomics research: Identification of trace-level protein digests and affinity capture of target peptides *Molecular & Cellular Proteomics 1(2),* pp. 157-168. 2002.

[14] F. Lin, C. M. Nguyen, S. Wang, W. Saadi, S. P. Gross and N. L. Jeon. Neutrophil migration in opposing chemoattractant gradients using microfluidic chemotaxis devices *Ann. Biomed. Eng. 33(4),* pp. 475-482. 2005.

[15] M. Mak, C. A. Reinhart-King and D. Erickson. Microfabricated physical spatial gradients for investigating cell migration and invasion dynamics *PLoS One 6(6),* pp. e20825. 2011.

[16] R. S. Martin, P. D. Root and D. M. Spence. Microfluidic technologies as platforms for performing quantitative cellular analyses in an in vitro environment *Analyst 131(11),* pp. 1197. 2006.

[17] J. C. McDonald and G. M. Whitesides. Poly(dimethylsiloxane) as a material for fabricating microfluidic devices *Acc. Chem. Res. 35(7),* pp. 491-499. 2002.

[18] J. W. Park, B. Vahidi, A. M. Taylor, S. W. Rhee and N. L. Jeon. Microfluidic culture platform for neuroscience research *Nature Protocols 1(4),* pp. 2128-2136. 2006.

[19] W. J. Polacheck, R. Li, S. G. M. Uzel and R. D. Kamm. Microfluidic platforms for mechanobiology *Lab on a Chip 13(12),* pp. 2252. 2013.

[20] S. M. N. Rao, V. K. Lin, U. Tata, G. V. Raj, J. Hsieh, K. Nguyen and J. C. Chiao. Demonstration of cancer cell migration using a novel microfluidic device *Journal of Nanotechnology in Engineering and Medicine 1(2),* pp. 021003. 2010.

[21] S. Rao, U. Tata, V. Lin and J. Chiao. The migration of cancer cells in gradually varying chemical gradients and mechanical constraints *Micromachines 5(1),* pp. 13-26. 2014.

[22] W. Saadi, S. W. Rhee, F. Lin, B. Vahidi, B. G. Chung and N. L. Jeon. Generation of stable concentration gradients in 2D and 3D environments using a microfluidic ladder chamber *Biomed. Microdevices 9(5),* pp. 627-635. 2007.

[23] W. Saadi, S. J. Wang, F. Lin and N. L. Jeon. A parallel-gradient microfluidic chamber for quantitative analysis of breast cancer cell chemotaxis *Biomed. Microdevices 8(2),* pp. 109-118. 2006.

[24] S. K. Sia and G. M. Whitesides. Microfluidic devices fabricated in poly(dimethylsiloxane) for biological studies *Electrophoresis 24(21),* pp. 3563-3576. 2003.

[25] C. Situma, M. Hashimoto and S. A. Soper. Merging microfluidics with microarray-based bioassays *Biomol. Eng. 23(5),* pp. 213-231. 2006.

[26] J. D. Snyder and T. A. Desai. Microscale three-dimensional polymeric platforms for in vitro cell culture systems *Journal of Biomaterials Science, Polymer Edition 12(8),* pp. 921-932. 2001.

[27] U. Tata, S. M N Rao, A. Sharma, K. Pabba, K. Pokhrel, B. Adhikari, V. K Lin and J. Chiao. Study of lung-metastasized prostate cancer cell line chemotaxis to epidermal growth factor with a BIOMEMS device *Advances in Natural Sciences: Nanoscience and Nanotechnology 3(3),* pp. 035007. 2012.

[28] G. M. Walker, N. Monteiro-Riviere, J. Rouse and A. T. O'Neill. A linear dilution microfluidic device for cytotoxicity assays *Lab. Chip 7(2),* pp. 226-232. 2007.

[29] C. Iliescu, H. Taylor, M. Avram, J. Miao and S. Franssila. A practical guide for the fabrication of microfluidic devices using glass and silicon *Biomicrofluidics 6(1),* pp. 016505. 2012.

[30] S. Sukas, R. M. Tiggelaar, G. Desmet and H. J. Gardeniers. Fabrication of integrated porous glass for microfluidic applications *Lab. Chip 13(15),* pp. 3061-3069. 2013.

[31] X. Li, D. R. Ballerini and W. Shen. A perspective on paper-based microfluidics: Current status and future trends *Biomicrofluidics 6(1),* pp. 011301. 2012.

[32] D. M. Cate, J. A. Adkins, J. Mettakoonpitak and C. S. Henry. Recent developments in paper-based microfluidic devices *Anal. Chem. 87(1),* pp. 19-41. 2015.

[33] A. W. Martinez, S. T. Phillips, G. M. Whitesides and E. Carrilho. Diagnostics for the developing world: Microfluidic paper-based analytical devices *Anal. Chem. 82(1),* pp. 3-10. 2010.

[34] A. K. Yetisen, M. S. Akram and C. R. Lowe. Paper-based microfluidic point-of-care diagnostic devices *Lab. Chip 13(12),* pp. 2210-2251. 2013.

[35] G. P. Gupta and J. Massagué. Cancer metastasis: Building a framework *Cell 127(4),* pp. 679-695. 2006.

[36] S. Valastyan and R. A. Weinberg. Tumor metastasis: Molecular insights and evolving paradigms *Cell 147(2),* pp. 275-292. 2011.

[37] P. S. Steeg. Tumor metastasis: Mechanistic insights and clinical challenges *Nat. Med. 12(8),* pp. 895-904. 2006.

[38] M. G. Mendez, S. Kojima and R. D. Goldman. Vimentin induces changes in cell shape, motility, and adhesion during the epithelial to mesenchymal transition *FASEB J. 24(6),* pp. 1838-1851. 2010.

[39] M. I. Kokkinos, R. Wafai, M. K. Wong, D. F. Newgreen, E. W. Thompson and M. Waltham. Vimentin and epithelial-mesenchymal transition in human breast cancer--observations in vitro and in vivo *Cells Tissues Organs 185(1-3),* pp. 191-203. 2007.

[40] A. J. Ewald, R. J. Huebner, H. Palsdottir, J. K. Lee, M. J. Perez, D. M. Jorgens, A. N. Tauscher, K. J. Cheung, Z. Werb and M. Auer. Mammary collective cell migration involves transient loss of epithelial features and individual cell migration within the epithelium *J. Cell. Sci. 125(Pt 11),* pp. 2638-2654. 2012.

[41] P. Friedl and S. Alexander. Cancer invasion and the microenvironment: Plasticity and reciprocity *Cell 147(5),* pp. 992-1009. 2011.

[42] P. Friedl and D. Gilmour. Collective cell migration in morphogenesis, regeneration and cancer *Nat. Rev. Mol. Cell Biol. 10(7),* pp. 445-457. 2009.

[43] P. Friedl, J. Locker, E. Sahai and J. E. Segall. Classifying collective cancer cell invasion *Nat. Cell Biol. 14(8),* pp. 777-783. 2012.

[44] P. Friedl, E. Sahai, S. Weiss and K. M. Yamada. New dimensions in cell migration *Nat. Rev. Mol. Cell Biol. 13(11),* pp. 743-747. 2012.

[45] P. Friedl and J. A. Zallen. Dynamics of cell-cell and cell-matrix interactions in morphogenesis, regeneration and cancer *Curr. Opin. Cell Biol. 22(5),* pp. 557-559. 2010.

[46] M. Inaki, S. Vishnu, A. Cliffe and P. Rorth. Effective guidance of collective migration based on differences in cell states *Proc. Natl. Acad. Sci. U. S. A. 109(6),* pp. 2027-2032. 2012.

[47] O. Ilina and P. Friedl. Mechanisms of collective cell migration at a glance *J. Cell. Sci. 122(Pt 18),* pp. 3203-3208. 2009.

[48] M. Poukkula, A. Cliffe, R. Changede and P. Rorth. Cell behaviors regulated by guidance cues in collective migration of border cells *J. Cell Biol. 192(3),* pp. 513-524. 2011.

[49] P. Rorth. Fellow travellers: Emergent properties of collective cell migration *EMBO Rep. 13(11),* pp. 984-991. 2012.

[50] P. Rorth. Whence directionality: Guidance mechanisms in solitary and collective cell migration *Dev. Cell. 20(1),* pp. 9-18. 2011.

[51] K. Wolf, S. Alexander, V. Schacht, L. M. Coussens, U. H. von Andrian, J. van Rheenen, E. Deryugina and P. Friedl. Collagen-based cell migration models in vitro and in vivo *Semin. Cell Dev. Biol. 20(8),* pp. 931-941. 2009.

[52] J. D. Shields, M. E. Fleury, C. Yong, A. A. Tomei, G. J. Randolph and M. A. Swartz. Autologous chemotaxis as a mechanism of tumor cell homing to lymphatics via interstitial flow and autocrine CCR7 signaling. *Cancer Cell 11(6),* pp. 526-538. 2007.

[53] E. T. Roussos, J. S. Condeelis and A. Patsialou. Chemotaxis in cancer *Nat. Rev. Cancer. 11(8),* pp. 573-587. 2011.

[54] H. C. Chen. Boyden chamber assay *Methods Mol. Biol. 294*pp. 15-22. 2005.

[55] D. Zicha, G. Dunn and G. Jones. Analyzing chemotaxis using the dunn direct-viewing chamber *Methods Mol. Biol. 75,* pp. 449-457. 1997.

[56] D. Zicha, G. A. Dunn and A. F. Brown. A new direct-viewing chemotaxis chamber *J. Cell. Sci. 99(4),* pp. 769-775. 1991.

[57] M. Vinci, C. Box, M. Zimmermann and S. A. Eccles. Tumor spheroid-based migration assays for evaluation of therapeutic agents. *Methods Mol. Biol. 986,* pp. 253-266. 2013.

[58] M. Vinci, S. Gowan, F. Boxall, L. Patterson, M. Zimmermann, W. Court, C. Lomas, M. Mendiola, D. Hardisson and S. A. Eccles. Advances in establishment and analysis of three-dimensional tumor spheroid-based functional assays for target validation and drug evaluation *BMC Biol. 10,* pp. 29-7007-10-29. 2012.

[59] C. Liang, A. Y. Park and J. Guan. In vitro scratch assay: A convenient and inexpensive method for analysis of cell migration in vitro *Nature Protocols 2(2),* pp. 329-333. 2007.

[60] S. Kim, H. J. Kim and N. L. Jeon. Biological applications of microfluidic gradient devices *Integr. Biol. (Camb) 2(11-12),* pp. 584-603. 2010.

[61] Y. Shin, S. Han, J. S. Jeon, K. Yamamoto, I. K. Zervantonakis, R. Sudo, R. D. Kamm and S. Chung. Microfluidic assay for simultaneous culture of multiple cell types on surfaces or within hydrogels *Nature Protocols 7(7),* pp. 1247-1259. 2012.

[62] B. G. Chung, A. Manbachi, W. Saadi, F. Lin, N. L. Jeon and A. Khademhosseini. A gradient-generating microfluidic device for cell biology *J. Vis. Exp. 7.* pp. 271. 2007.

[63] Q. Kong, R. A. Able Jr, V. Dudu and M. Vazquez. A microfluidic device to establish concentration gradients using reagent density differences *J. Biomech. Eng. 132(12),* pp. 121012. 2010.

[64] U. S. Tata. Micromachined devices for in vitro biomedical applications. *ProQuest Dissertations and Theses* 2012.

[65] S. Malalur Nagaraja Rao. A microfluidic platform to study cell migration. *ProQuest Dissertations and Theses* 2009.

[66] W. Nusselt. *Das Grundgesetz Des Wärmeüberganges*. 1915.

[67] J. R. Molina, P. Yang, S. D. Cassivi, S. E. Schild and A. A. Adjei. Non-small cell lung cancer: Epidemiology, risk factors, treatment, and survivorship *Mayo Clin. Proc. 83(5),* pp. 584-594. 2008.

[68] C. S. Dela Cruz, L. T. Tanoue and R. A. Matthay. Lung cancer: Epidemiology, etiology, and prevention *Clin. Chest Med. 32(4),* pp. 605-644. 2011.

[69] Bethune, G., Bethune, D., Ridgway, N., Xu,Z. Epidermal growth factor receptor (EGFR) in lung cancer: An overview and update. *Journal of Thoracic Disease 2(1),* 2011.

[70] S. M. Lee. Is EGFR expression important in non-small cell lung cancer? *Thorax 61(2),* pp. 98-99. 2006.

[71] B. D. Lehmann and J. A. Pietenpol. Identification and use of biomarkers in treatment strategies for triple-negative breast cancer subtypes *J. Pathol. 232(2),* pp. 142-150. 2014.

[72] K. Roepstorff, L. Grovdal, M. Grandal, M. Lerdrup and B. van Deurs. Endocytic downregulation of ErbB receptors: Mechanisms and relevance in cancer *Histochem. Cell Biol. 129(5),* pp. 563-578. 2008.

[73] R. Siegel, J. Ma, Z. Zou and A. Jemal. Cancer statistics, 2014 *CA: A Cancer Journal for Clinicians 64(1),* pp. 9-29. 2014.

[74] G. Gandaglia, F. Abdollah, J. Schiffmann, V. Trudeau, S. F. Shariat, S. P. Kim, P. Perrotte, F. Montorsi, A. Briganti, Q. D. Trinh, P. I. Karakiewicz and M. Sun. Distribution of metastatic sites in patients with prostate cancer: A population-based analysis *Prostate 74(2),* pp. 210-216. 2014.

[75] Y. Qiu, Z. Y. Zhang, W. D. Du, L. Ye, S. Xu, X. B. Zuo, F. S. Zhou, G. Chen, X. L. Ma, M. E. Schneider, H. Z. Xia, Y. Zhou, J. F. Wu, X. Yuan-Hong and X. J. Zhang. Association analysis of ERBB2 amplicon genetic polymorphisms and STARD3 expression with risk of gastric cancer in the chinese population *Gene 535(2),* pp. 225-232. 2014.

[76] E. Katz, S. Dubois-Marshall, A. H. Sims, D. Faratian, J. Li, E. S. Smith, J. A. Quinn, M. Edward, R. R. Meehan, E. E. Evans, S. P. Langdon and D. J. Harrison. A gene on the HER2 amplicon, C35, is an oncogene in breast cancer whose actions are prevented by inhibition of syk *Br. J. Cancer 103(3),* pp. 401-410. 2010.

[77] C. J. Yang, C. F. Chang, L. Y. Huang, Y. Y. Chang, T. L. Shen and C. H. Hsu. Resonance assignments of human C35 (C17orf37) protein, a novel tumor biomarker *Biomol. NMR Assign 4(2),* pp. 191-193. 2010.

[78] S. Dasgupta, L. M. Wasson, N. Rauniyar, L. Prokai, J. Borejdo and J. K. Vishwanatha. Novel gene C17orf37 in 17q12 amplicon promotes migration and invasion of prostate cancer cells *Oncogene 28(32),* pp. 2860-2872. 2009.

[79] E. E. Evans, A. D. Henn, A. Jonason, M. J. Paris, L. M. Schiffhauer, M. A. Borrello, E. S. Smith, D. M. Sahasrabudhe and M. Zauderer. C35 (C17orf37) is a novel tumor biomarker abundantly expressed in breast cancer *Mol. Cancer. Ther. 5(11),* pp. 2919-2930. 2006.

[80] T. H. Leung, S. C. Wong, K. K. Chan, D. W. Chan, A. N. Cheung and H. Y. Ngan. The interaction between C35 and DeltaNp73 promotes chemo-resistance in ovarian cancer cells *Br. J. Cancer 109(4),* pp. 965-975. 2013.

[81] S. Dasgupta, I. Cushman, M. Kpetemey, P. J. Casey and J. K. Vishwanatha. Prenylated c17orf37 induces filopodia formation to promote cell migration and metastasis *J. Biol. Chem. 286(29),* pp. 25935-25946. 2011.

[82] C. H. Hsu, T. L. Shen, C. F. Chang, Y. Y. Chang and L. Y. Huang. Solution structure of the oncogenic MIEN1 protein reveals a thioredoxin-like fold with a redox-active motif *PLoS One 7(12),* pp. e52292. 2012.

[83] A. Mócsai, C. L. Abram, Z. Jakus, Y. Hu, L. L. Lanier and C. A. Lowell. Integrin signaling in neutrophils and macrophages uses adaptors containing immunoreceptor tyrosine-based activation motifs. *Nat. Immunol. 7(12),* pp. 1326-1333. 2006.

[84] L. L. Lanier, B. C. Corliss, J. Wu, C. Leong and J. H. Phillips. Immunoreceptor DAP12 bearing a tyrosine-based activation motif is involved in activating NK cells. *Nature 391(6668),* pp. 703-707. 1998.

[85] S. Fruehling and R. Longnecker. The immunoreceptor tyrosine-based activation motif of Epstein–Barr virus LMP2A is essential for blocking BCR-mediated signal transduction. *Virology 235(2),* pp. 241-251. 1997.

[86] B. Lowin-Kropf, V. S. Shapiro and A. Weiss. Cytoskeletal polarization of T cells is regulated by an immunoreceptor tyrosine-based activation motif-dependent mechanism. *J. Cell Biol. 140(4),* pp. 861-871. 1998.

[87] S. Rajendiran, A. V. Parwani, R. J. Hare, S. Dasgupta, R. K. Roby and J. K. Vishwanatha. MicroRNA-940 suppresses prostate cancer migration and invasion by regulating MIEN1 *Mol. Cancer. 13(250)*. 2014.

[88] K. V. Nguyen-Ngoc, K. J. Cheung, A. Brenot, E. R. Shamir, R. S. Gray, W. C. Hines, P. Yaswen, Z. Werb and A. J. Ewald. ECM microenvironment regulates collective migration and local dissemination in normal and malignant mammary epithelium *Proc. Natl. Acad. Sci. U. S. A. 109(39),* pp. E2595-604. 2012.

[89] A. Bianco, M. Poukkula, A. Cliffe, J. Mathieu, C. M. Luque, T. A. Fulga and P. Rorth. Two distinct modes of guidance signalling during collective migration of border cells *Nature 448(7151),* pp. 362-365. 2007.

Biographical Information

Lyndon Lee was born in Arlington, Texas. He received his B.S. in biomedical engineering from the University of Texas at Austin in 2013. He received his M.S. in bioengineering from the University of Texas at Arlington in 2015. His current research interests include developing models to study cellular migration phenomena.